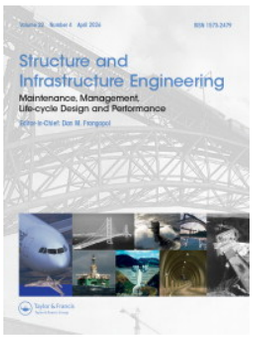

Taylor & Francis
Taylor & Francis Group

Structure and Infrastructure Engineering
Maintenance, Management, Life-Cycle Design and Performance

ISSN: 1573-2479 (Print) 1744-8980 (Online) Journal homepage: www.tandfonline.com/journals/nsie20

High-fidelity analysis of service life extension for steel beam bridges retrofitted with external adaptive tensioning systems

Dshamil Efinger , Khairina A. Canny , Martin Dazer , Lucio Blandini & Gennaro Senatore

To cite this article: Dshamil Efinger , Khairina A. Canny , Martin Dazer , Lucio Blandini & Gennaro Senatore (19 Mar 2026): High-fidelity analysis of service life extension for steel beam bridges retrofitted with external adaptive tensioning systems, Structure and Infrastructure Engineering, DOI: 10.1080/15732479.2026.2631164

To link to this article: https://doi.org/10.1080/15732479.2026.2631164

Published online: 19 Mar 2026.

STRUCTURE AND INFRASTRUCTURE ENGINEERING
https://doi.org/10.1080/15732479.2026.2631164

High-fidelity analysis of service life extension for steel beam bridges retrofitted with external adaptive tensioning systems

Dshamil Efinger[a], Khairina A. Canny[b], Martin Dazer[a], Lucio Blandini[b] and Gennaro Senatore[b]

[a]Institute of Machine Components (IMA), University of Stuttgart, Stuttgart, Germany; [b]Institute for Lightweight Structures and Conceptual Design (ILEK), University of Stuttgart, Stuttgart, Germany

ABSTRACT

This study investigates the use of External Adaptive Tensioning (EAT) systems as a retrofit strategy to reduce the structural response and fatigue damage in steel bridges. A high-fidelity three-dimensional model, including detailed welded-joint sub-models, is combined with the Active System Utilisation (ASU) metric to account for actuator reliability and fallback configurations. Results show that EAT reduces the stress response by up to 66% relative to the unretrofitted condition and achieves near-zero fatigue damage at critical welded details under representative traffic loading. Even with partial downtime (ASU < 1), EAT provides substantial gains in remaining service life compared with passive external post-tensioning. These findings demonstrate the structural benefits of retrofitting with active components and establish a computational framework for evaluating fatigue and reliability effects in actively controlled bridge systems.

ARTICLE HISTORY
Received 21 August 2025
Revised 20 December 2025
Accepted 19 January 2026

KEYWORDS
Active structural control; adaptive structures; bridge retrofitting; fail-safe design; fatigue damage mitigation; fatigue life extension; reliability assessment; steel bridges

1. Introduction

The growing global demand for bridge retrofitting is primarily driven by ageing infrastructure. In many countries, approximately 40–50% of bridges have exceeded their intended service life of 50 years (Frangopol & Kim, 2022). Ageing structures face challenges including corrosion-induced material deterioration (Li et al., 2025), increased loads beyond original design assumptions (Kalkowsky et al., 2024), and fatigue damage from repeated stress cycles (Eberle & Oberguggenberger, 2023). Many older bridges also fail to meet modern safety and functionality standards. Environmental factors such as harsh weather and de-icing salts accelerate degradation, while detecting hidden damage requires advanced inspection technologies (Yoon et al., 2022). These issues pose significant safety and economic risks, highlighting the urgency for innovative retrofitting, reliable monitoring, and predictive maintenance to sustain critical infrastructure (van Dinter et al., 2022). Fatigue is a particularly critical concern for steel bridges, arising from repetitive loading by traffic, wind, and environmental effects (Du et al., 2024). Welded and bolted connections, as well as stress concentration zones like joints and stiffeners, are especially susceptible (Bertolesi et al., 2021). If unaddressed, fatigue can lead to catastrophic failures, threatening safety and transport continuity (Wu et al., 2018). Effective monitoring, maintenance, and retrofitting strategies are essential to mitigate fatigue-related deterioration and extend service life.

Conventional retrofit methods for steel bridges typically involve adding materials or elements to restore or enhance capacity (Fatemi et al., 2011), including external post-tensioning, steel plate bonding, and composite reinforcements (Zhang et al., 2021). While effective against issues such as settlement, cracking, or construction defects, these approaches have limitations. Steel plates and jacketing may improve strength yet fail to mitigate fatigue or corrosion, particularly in chloride-rich environments, and can obscure existing damage, complicating inspections (Soliman & Frangopol, 2015). Their effectiveness is generally constrained under unforeseen loading and heavily reliant on timely damage detection (Avci et al., 2021). Moreover, adding or replacing structural components can introduce unintended stress concentrations that exacerbate existing weaknesses (Delzendeh Moghadam et al., 2024). Heavy reinforcements may alter stress distributions, creating new failure points (R. Wang, Leander, et al., 2023). For example, retrofitting in a Mississippi River bridge accelerated fatigue crack propagation, leading to a deck beam failure (Horgan, 2021). A more critical case was the 1996 collapse of the Koror–Babeldaob Bridge in Palau, caused by a retrofit that removed the central hinge and added post-tensioned continuity, imposing concentrated compressive forces on an under-reinforced top flange (Burgoyne & Scantlebury, 1996). This intervention transformed a stable hinged system into a statically indeterminate structure, where stress redistribution and progressive delamination led to loss of composite action and ultimate

CONTACT Gennaro Senatore gennaro.senatore@ilek.uni-stuttgart.de Institute for Lightweight Structures and Conceptual Design (ILEK), University of Stuttgart, Stuttgart, Germany.

shear failure within weeks (Bažant et al., 2012). This case highlights that inadequate understanding of existing stresses and material degradation can turn a retrofit into a source of failure rather than repair.

Alternative strategies include passive, semi-active, and active control systems. Passive devices such as viscous, friction, and metallic dampers are installed in bracing or key connections to dissipate energy (Tell et al., 2021). Buckling-restrained braces (BRBs) improve ductility under cyclic loads (Wei et al., 2019), while tuned mass dampers (TMDs) and slosh tanks mitigate wind and seismic vibrations by transferring energy from the primary structure (Møller et al., 2019). Recent developments, such as tuned mass damper inerters (TMDIs) (B. Chen et al., 2022) and specially configured viscous dampers (C. Yang et al., 2024), offer enhanced performance over a broader excitation range, bridging the gap between traditional passive and more adaptive systems, yet still lack real-time adjustability. Semi-active devices adjust stiffness and damping properties in real time, acting as programmable passive systems (Gkatzogias & Kappos, 2016). Deployments like magnetorheological (MR) bearings on the Dongting Lake Bridge reduced stress ranges by about 25%, delaying fatigue initiation (Z. Q. Chen et al., 2003). Variable stiffness bearings similarly enhance vibration control and load redistribution by dynamically adapting to loads (Cao et al., 2022). Adjustable joints in buildings and bridges have also demonstrated substantial vibration mitigation under varied scenarios (Q. Wang et al., 2021). Nonetheless, under extreme events such as strong earthquakes, severe winds, or heavy overloading, passive and semi-active systems may provide insufficient protection, given their limited adaptability to changing loads or evolving structural conditions and their tendency to impose localised force demands that require careful detailing (Banerjee et al., 2025; Saeed et al., 2023).

Active control strategies surpass passive approaches by employing feedback systems that adapt in real time. Recent applications include aerodynamic flaps to suppress wind-induced flutter in long-span bridges (Z. Wang, Zhao, et al., 2023) and active tuned mass dampers (ATMDs) to control vortex-induced vibrations (Dai et al., 2022), illustrating active systems' superior adaptability. Integrated structure-control designs have achieved significant reductions in mass and embodied carbon for high-rise buildings (Senatore et al., 2025) and long-span floor slabs (Reksowardojo et al., 2024a) relative to optimised passive solutions. By actively adjusting the response of the structure, actuators lessen reliance on material-based stiffness and strength. Topology-optimised adaptive structures achieve exceptional material efficiency while meeting strength and serviceability requirements – outcomes unattainable without adaptivity (Senatore & Wang, 2024). This approach leverages modest operational energy, deployed selectively during critical events, optimising total energy demands encompassing both embodied and operational shares (Reksowardojo & Senatore, 2023).

External post-tensioning has long been applied to mitigate structural damage in beam bridges by introducing compressive forces through high-strength tendons. While effective in enhancing load capacity and extending service life, these conventional approaches lack adaptivity, often failing to address localised deterioration under evolving load demands or material degradation (Alsharari et al., 2021). In contrast, External Adaptive Tensioning (EAT) systems integrate under-deck cables guided by linear actuators that dynamically adjust to reduce displacements and redistribute stress. Previous numerical investigations into EAT systems have demonstrated their potential to enhance the global dynamic performance of bridges. Reksowardojo et al. (Reksowardojo et al., 2024b) formulated a computational methodology for the design and control of single-span high-speed railway bridges equipped with EAT, employing a simplified two-dimensional representation to evaluate dynamic performance and control effectiveness. The study demonstrated that EAT can effectively suppress resonance at critical train–bridge velocities, maintaining mid-span deflections within serviceability limits. A complementary parametric investigation across different span lengths (20, 30, and 40 m) further showed that EAT can enable longer spans and lighter superstructures, with the largest mass reduction of about 32% achieved for the 40 m span compared with the equivalent passive design.

Dakova et al. (2023) proposed a model-predictive-control strategy for EAT using a simplified two-dimensional model of a simply supported 40 m steel railway bridge with three actuated under-deck struts. Simulations under Eurocode 1 (CEN, 2003) train loading showed that EAT reduced vibration amplitudes by up to 65%, corresponding to an effective $\approx$ 50% increase in damping, while keeping actuator forces within practical limits ($\approx$ 200–285 kN). Using the same 40 m single span bridge model, Zeller et al. (2023) developed a state- and disturbance-estimation framework for EAT-equipped railway bridges. Closed-loop simulations combining an augmented Kalman filter with LQR control showed that EAT reduced vibration amplitudes by up to 53% using estimated states, confirming that accurate online estimation can enable effective real-time control and enhanced damping performance without requiring full-state measurements. Canny et al. (2025) applied EAT to an existing prestressed-concrete bridge to recover long-term prestress losses and reduce service-load effects. Using a two-dimensional finite-element model, they found that EAT restored near-original tendon forces, reducing peak bending moments local stress ranges in the deck and anchor zones by about 20% relative to the unretrofitted condition. The study focused on static performance recovery and did not address dynamic, fatigue, or reliability aspects. Generally, prior work has shown that while well-designed actuation reduces global stresses, localised stress increases may arise near actuator connections, necessitating more detailed analyses to prevent unintended damage (Efinger et al., 2022).

2. New contribution

Previous investigations into EAT systems have focused primarily on idealised or newly designed bridges, without assessing their use as retrofitting strategies for existing

structures. None of these studies considered weld/stiffener details or actuator–structure interfaces to quantify potential service-life extension through fatigue-damage reduction, nor did they consider system reliability, as continuous, failure-free operation of the active components was generally assumed. Table 1 summarises the scope of the studies most directly related to this work. The present study closes these gaps by integrating high-fidelity 3D modelling of welded and actuator-interface details with a reliability-informed assessment based on Active System Utilisation (ASU) and explicitly defined fallback configurations. This study adopts a two-step control–simulation framework in which control forces are first computed using a reduced-order two-dimensional model and subsequently applied to the high-fidelity three-dimensional model. This hierarchical approach captures the controlled structural response with geometric detail while keeping computational demands tractable, providing an effective balance between modelling accuracy and efficiency. This approach enables a fatigue-based life-extension evaluation of an EAT-retrofitted steel bridge under realistic operational conditions.

This work makes several novel contributions that systematically address these shortcomings:

- **High-fidelity fatigue analysis:** this study is the first to quantify EAT effectiveness in mitigating fatigue damage in steel bridges by explicitly modelling geometric discontinuities, including welds, stiffeners, cut-outs, and actuator-structure interfaces, through refined shell and sub-models, thereby achieving a level of detail well beyond conventional global beam or shell models.
- **Detailed local stress assessment:** demonstrates that EAT reduces von Mises stresses by up to 66% compared to the non-retrofitted case and by 43% relative to an equivalent external post-tensioning system without actuators, here referred to as 'passive' (EPT), while accurately capturing shear lag and local stress amplification effects.
- **Robust fatigue life quantification:** shows that for critical fatigue-prone locations, EAT reduces damage accumulation to near zero under typical operational scenarios, resulting in substantial theoretical Remaining Useful Life (RUL) extensions well beyond those achievable with conventional measures, where EPT, for comparison, may locally extend life by factors up to ∼5.8 under specific conditions, but with less uniformity and potential drawbacks at other points.
- **Integration of operational reliability:** introduces the concept of Active System Utilisation (ASU) to explicitly quantify the impact of EAT system availability on fatigue performance, assessing fallback scenarios (partial or complete loss of active functionality) and their effects on long-term service life.
- **Clear durability benchmarking:** establishes a structured comparative framework that quantifies the added value of adaptive retrofit strategies over conventional approaches in fatigue-critical steel bridge applications.

By addressing these aspects within a unified high-fidelity and reliability-informed framework, this study significantly advances the understanding of EAT systems' long-term effectiveness in extending the service life of ageing steel infrastructure.

3. System description

3.1. Methodology

To assess the effect of actuation on the bridge response using a high-fidelity model, a framework is developed based on the methodology initially established for a 2D model. A flowchart of this methodology, tailored to the case study examined in this work, is presented in Figure 1. For simplicity, a simply supported steel box-girder bridge is considered. However, the methodology can be applied to other bridge types. The framework incorporates order reduction by deriving control inputs from the 2D model and subsequently extending them to the 3D model.

Given the increased complexity associated with the 3D model, detailed design of the actuator components is required, including connections and interfaces with the housing elements and the beam bridge. Parameters from the 2D model are adjusted to closely align with the behaviour of the 3D model, ensuring consistency between the two. This two-step approach offers a practical balance between computational efficiency and modelling accuracy, avoiding the high computational cost associated with solving the full control problem directly in 3D, which involves a significantly greater number of degrees of freedom and integration points. The following sections detail the structural system, control strategy, and damage assessment methodology, providing a comprehensive overview of the approach employed.

3.2. External adaptive tensioning vs external passive tensioning

This section introduces the three key configurations through a conceptual yet analytical examination of their distinct structural behaviour, namely the unretrofitted state, the

Table 1. Scope of previous EAT studies and aspects addressed in this work.

Study	Model fidelity	Fatigue / durability assessment	Reliability / fallback considered	Retrofit analysed
Reksowardojo et al. (2024b)	2D simplified dynamic model	No, global response	No	No, new design
Dakova et al. (2023)	2D simplified dynamic model	No, global response	No	No, new design
Zeller et al. (2023)	2D simplified dynamic model	No, global response	No	No, new design
Canny et al. (2025)	2D simplified static model	No, static analysis	No	Yes, existing structure
This study	3D shell + sub-model representation	Yes, detail-resolved fatigue and RUL evaluation	Yes, ASU-based reliability + fallback	Yes, explicit retrofit

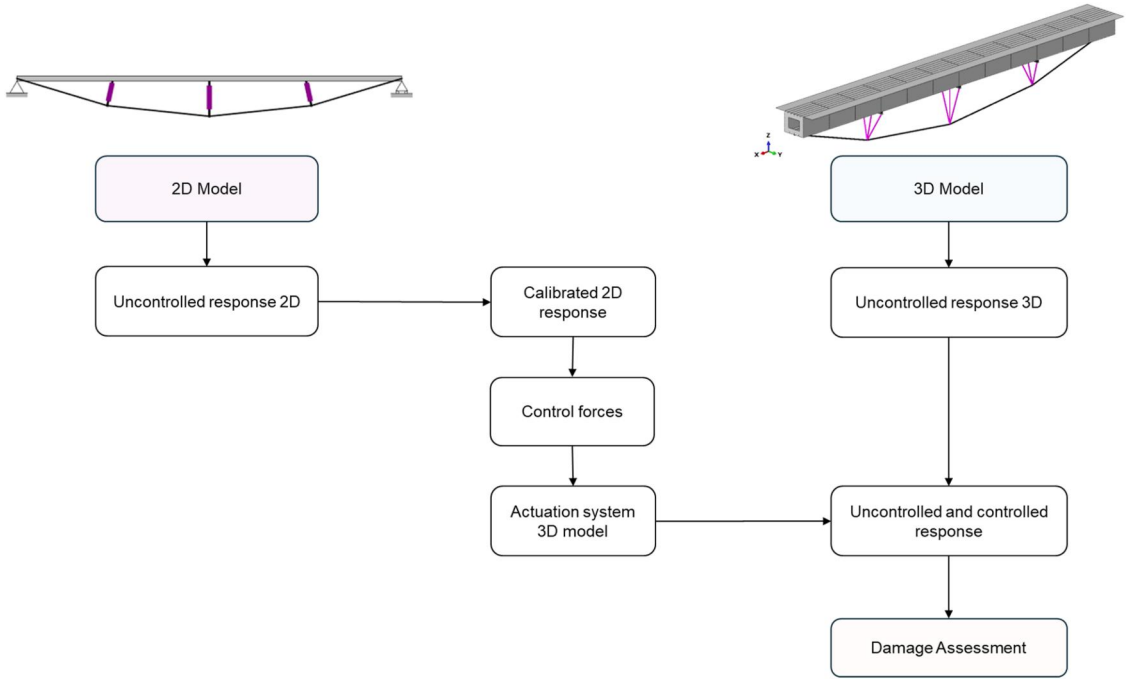

Figure 1. Flowchart methodology, actuators are represented with thicker purple lines.

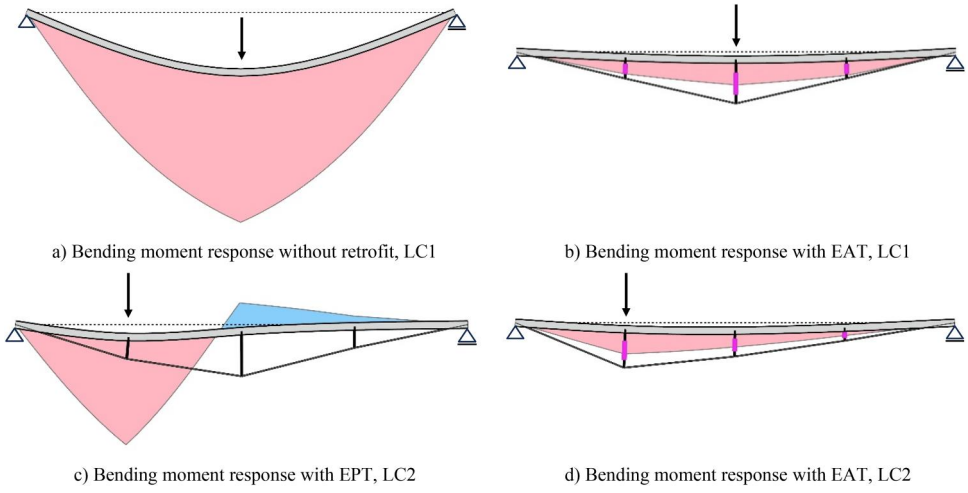

Figure 2. Benchmark bending moment response: no retrofit, EAT and EPT.

bridge retrofitted with external post-tensioning or External Passive Tensioning (EPT), and the bridge equipped with External Adaptive Tensioning (EAT). Figure 2 illustrates a benchmark comparison of the bending moment response under moving loads for these three configurations. Two load cases are considered: LC1, representing the train positioned at mid-span, and LC2, with the train located at quarter span. The results clearly show that the EAT system significantly reduces the bending moment response compared to both the unretrofitted case and the EPT system. In the EAT configuration, the struts effectively act as intermediate supports. Their ability to adjust length dynamically enables substantial reduction of mid-span bending moments without inducing unintended stress increases elsewhere, such as at the quarter and three-quarter spans where the other struts are located. This is evident when comparing the bending moment response under LC1 for EPT (Figure 2a) and EAT (Figure 2b), where the adaptive system achieves a markedly lower stress level.

EPT is typically employed as a global remedial measure. However, it may not sufficiently address localised damage or deterioration, which often requires targeted load redistribution to critical structural members. In cases where original members are already compromised, EPT alone may fail to achieve the necessary redistribution. Because the EPT configuration remains unchanged under different load positions, it performs poorly under LC2, when the load is at quarter span. Here, the stress reduction is ineffective near the load application, and stress reversal occurs, evidenced by the negative bending moments (placing the top fibre in tension) shown in blue in Figure 2c. This unintended behaviour can exacerbate fatigue-induced damage and deterioration. In contrast, the

EAT system's ability to adapt strut lengths in response to moving loads ensures efficient stress reduction even under LC2 conditions, as demonstrated in Figure 2d. This highlights the superior capacity of the adaptive system to mitigate stresses dynamically and protect the structure from localised fatigue damage.

3.3. Structural-control system

A simply supported steel box-girder beam bridge is considered. The bridge is assumed to be retrofitted with an External Adaptive Tensioning (EAT) system, comprising three strut-actuator assemblies that deviate a cable connected to the ends of the beam bridge. The actuators are installed in series with their housing element. In this configuration, the housing element and the actuator are subjected to the same force. Table 2 presents a conceptual framework of the response states analysed in this study, along with their corresponding loading conditions. The conceptualisation of these states builds upon a framework similar to that established in previous studies (Canny et al., 2025), which is briefly summarised here for the sake of completeness and to ensure clarity of notation. The bridge response before retrofitting is characterised by two deformation states:

a. The deformation state under permanent loads $\mathbf{p}^{sw} + \mathbf{p}^{dl}$ (self-weight and dead load).
b. The deformation state under the combined effects of permanent and train loads $\mathbf{p}^{t}(t)$.

When the bridge is retrofitted with an EAT system, the states are:

c. The uncontrolled state under permanent load.
d. The initial pretension state under permanent loads. This is conceptualised as a prestressed state achieved through a one-time external actuation (e.g. jacks) $\mathbf{p}^{ps}$, compensating for the effects of permanent loads and preventing sagging in the cables. For clarity, it is assumed that the train enters the bridge in this prestressed state. This state also represents the bridge retrofitted with an External Passive Tensioning (EPT) system.
e. The uncontrolled state under train load, where no actuator force $\mathbf{p}^{act}(t)$ is applied, resulting in a typical response due to the train load.
f. The controlled state under train load, where actuator forces $\mathbf{p}^{act}(t)$ are applied to reduce the response induced by the train load.

These states provide a structured framework for evaluating the effectiveness of the EAT system in minimising the bridge's structural response, with the ultimate goal of mitigating fatigue-induced damage.

Table 2. Structure-control system states, actuators represented with thicker purple lines.

	State	Loads
No retrofit	 a) Response under permanent load	$\mathbf{p}^{sw} + \mathbf{p}^{dl}$
	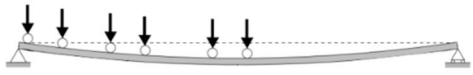 b) Response under train load	$\mathbf{p}^{sw} + \mathbf{p}^{dl} + \mathbf{p}^{t}(t)$
EAT retrofit	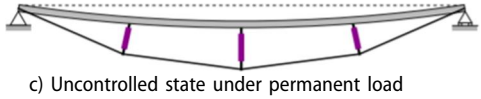 c) Uncontrolled state under permanent load	$\mathbf{p}^{sw} + \mathbf{p}^{dl}$
	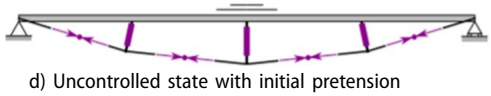 d) Uncontrolled state with initial pretension	$\mathbf{p}^{0} = \mathbf{p}^{sw} + \mathbf{p}^{dl} + \mathbf{p}^{ps}$ $\mathbf{p}^{ps} = \Delta 1^{ps}$
	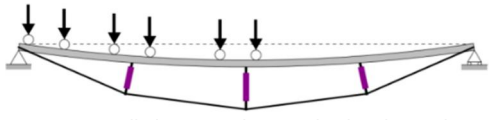 e) Uncontrolled state under train load with initial pretension	$\mathbf{p}^{nc}(t) = \mathbf{p}^{sw} + \mathbf{p}^{dl} + \mathbf{p}^{ps} + \mathbf{p}^{t}(t)$
	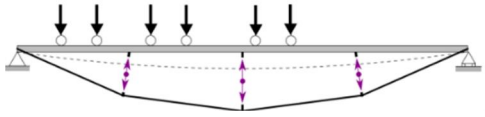 f) Controlled state under train load	$\mathbf{p}^{c}(t) = \mathbf{p}^{sw} + \mathbf{p}^{dl} + \mathbf{p}^{ps} + \mathbf{p}^{t}(t) + \mathbf{p}^{act}(t)$

3.4. FE model

The three-dimensional model of the bridge is developed using ABAQUS with the Dynamic Implicit solver to simulate the bridge response under external and actuation loads. The bridge is supported by pins on the left ends and rollers on the right end as depicted in Figure 3. The box girder consists of the deck, upper and lower flanges, webs, longitudinal stiffeners, and diaphragms. Each strut–actuator assembly includes three beam elements, each housing an actuator, as shown in Figure 3. To ensure effective load transfer and minimise stress concentrations at the actuator–structure interface, a capping beam is installed between the actuator housing and the lower flange of the girder. The system is configured to maintain structural stability under failure scenarios, ensuring no collapse occurs in the event of actuator malfunction or control system failure.

The box girder is modelled (Figure 4) using S4R shell elements four-node, reduced-integration shell elements that offer a balance of computational efficiency and structural accuracy. The struts and capping beams are represented with B31 beam elements, which are two-node linear interpolation elements suitable for 3D structural analysis. To avoid nonlinear effects from slackness, the cables are modelled using T3D2 truss elements, assuming continuous tension is maintained due to the initial prestressed state, thereby preventing load reversal. The upper slab is modelled as a composite system comprising a steel plate and a concrete layer. Tie constraints are applied between the actuator housing elements, the capping beam, and the lower flange of the bridge, as illustrated in Figure 5.

To take a conservative approach in modelling the 3D global behaviour, the tie constraint is restricted to the weld seamline (Figure 5c). This method reduces the load application region, resulting in higher stress concentrations, particularly in scenarios where the capping beam undergoes pull-out forces. By focusing on localised stress accumulation, this approach provides a conservative estimation of stress distribution, aiming to accurately capture variations in load transfer under both compressive and tensile loading conditions, such as when the capping beam is subjected to pull-out forces. To ensure a more accurate assessment of the actuator-bridge interface and evaluate potential failure mechanisms, a high-fidelity sub-model is implemented. This approach compensates for the limitations and reduced degrees of freedom inherent in the simplified model, which uses beam elements to represent the interface between the actuators and the bridge. This region is prone to multiple complex failure modes, necessitating a more detailed and accurate evaluation. The sub-model incorporates critical components such as welds and stiffeners. Kinematic conditions from the global model are applied to the sub-model to ensure consistency at the boundaries. The welding seamline is modelled in greater detail, physically representing the load transfer and stress distribution characteristics specific to a welded joint:

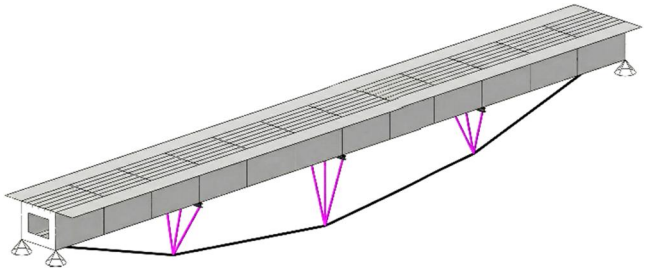

Figure 3. Support conditions, actuators represented with purple lines.

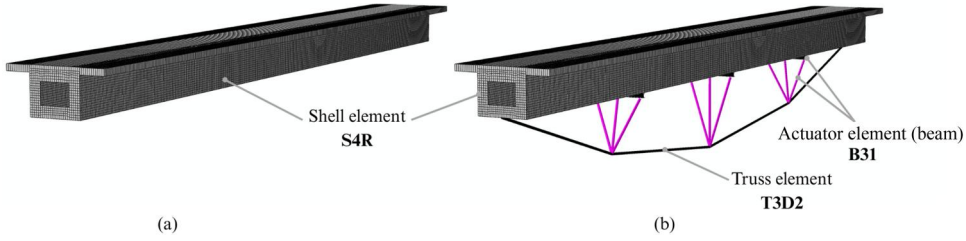

Figure 4. FE model, beam bridge (a) and equipped with EAT (b).

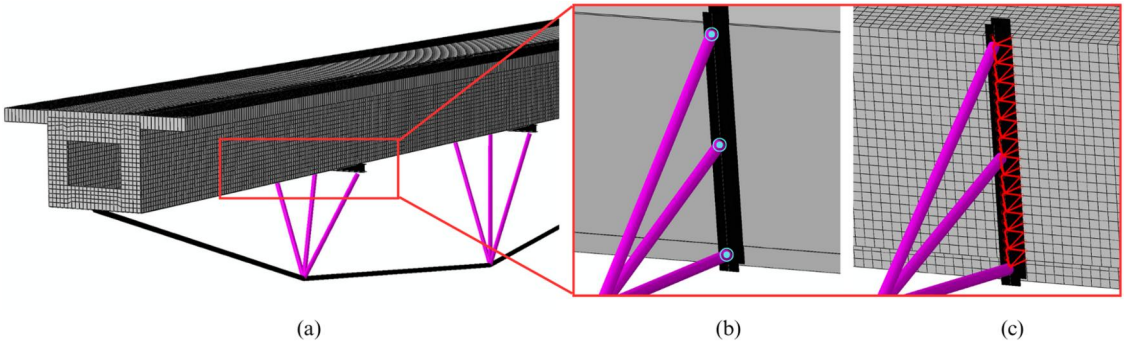

Figure 5. Tie constraint implementation: (a) constraint region; (b) actuator housing and capping beam; (c) capping beam and weld lines.

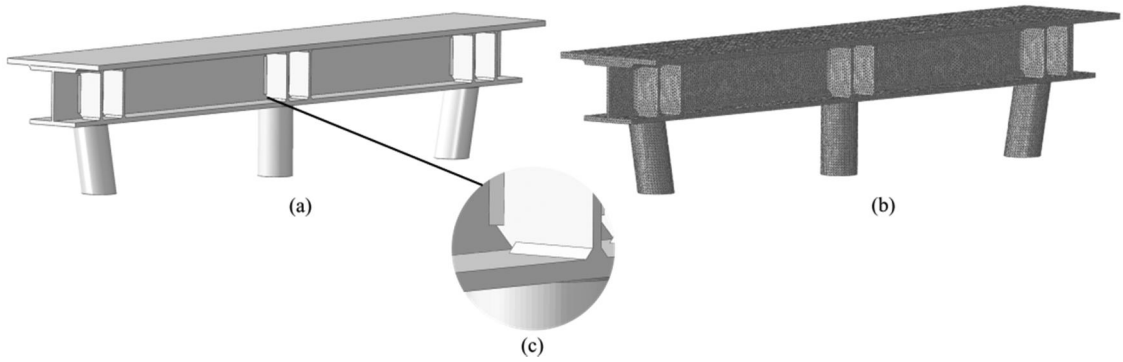

Figure 6. Sub-model of the actuator–structure interface: (a) capping beam and actuator housing; (b) refined mesh; (c) stiffener welds and cut-outs.

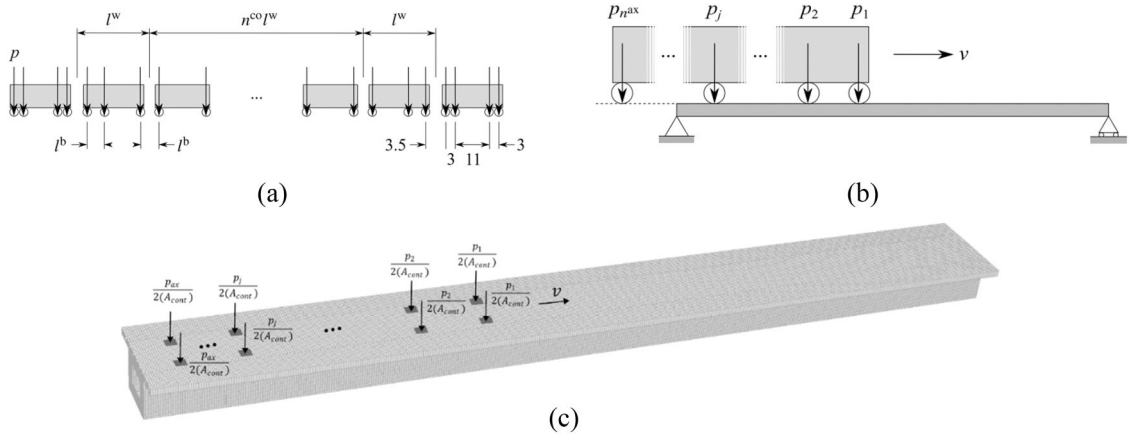

Figure 7. Train loads: (a) HSLM-A dimension in m; (b) point load in 2D; (c) distributed load in 3D.

- Under compressive loads, full contact is modelled between the elements,
- Under tensile loads, contact is concentrated along the weld seam.

Figure 6 shows the actuator-bridge interface sub-model, highlighting the detailed representation of the welds and surrounding components. The sub-model includes welds and cross-sectional elements illustrated in Figure 6b, which are modelled with C3D10 elements, a general-purpose tetrahedral element with four integration points. To address local buckling, two additional stiffeners are incorporated for each actuator housing element. To further enhance the design, cut-outs are introduced at the corners of the stiffeners and the capping beam to minimise stress concentrations and mitigate stress localisation effects (Figure 6c).

3.5. Loading conditions

The loading conditions are based on train loads specified by Eurocode 1 (CEN, 2003), specifically employing the High-Speed Load Model A (HSLM-A). These train loads are applied as moving point loads in 2D and moving distributed loads in 3D. The distributed loads are modelled as pressure loads applied to the upper flange of the beam bridge, simulating the load transfer from the train's axles. Figure 7 provides an illustration of the applied train loads.

The parameter n^{co} denotes the number of intermediate cars, l^b represents the wheel-to-bogey distance, and l^w indicates the length of the cars. For the distributed load in the 3D model, a contact area of 500 mm × 500 mm is assumed, with a track gauge spacing of 1,500 mm. Based on the HSLM-A parameters, multiple train types are analysed to identify the one that induces the highest stress response in the steel box girder deck. The T2 train type is selected for further analysis, as it results in the highest stress response in the uncontrolled state. The T2 train consists of $n^{co} = 17$ intermediate cars, each $l^w = 19{,}000$ mm long, with a wheel-to-bogey distance $l^b = 3{,}500$ mm and an axle load of $p = 200$ kN.

3.6. Computation of control inputs

The moving load on the bridge is modelled as a point load, excluding the effects of vehicle-bridge interaction. This study adopts a conservative approach by representing the vehicle load solely as a point force, thereby neglecting dynamic interactions such as vehicle suspension effects, road surface irregularities, and bridge deck flexibility. This simplification ensures a higher estimation of localised stress concentrations, providing a worst-case scenario assessment of the bridge's structural response. This assumption is consistent with the findings (Reksowardojo et al., 2024b), where coupled vehicle–bridge interaction simulations showed that the train suspension behaves as a dynamic damper, absorbing vibration energy

and thereby reducing bridge displacement and stress amplitudes compared with the moving-point-load model. The equation of motion under a moving point load is:

$$\mathbf{M}\ddot{\mathbf{d}}(t) + \mathbf{C}\dot{\mathbf{d}}(t) + \mathbf{K}\mathbf{d}(t) = \mathbf{p}^0 + \mathbf{p}^t(t) + \mathbf{p}^{act}(t) \tag{1}$$

where $\mathbf{M}, \mathbf{C}, \mathbf{K} \in \mathbb{R}^{n^d \times n^d}$ are the mass, damping, and stiffness matrix respectively. The terms $\mathbf{d}$, $\dot{\mathbf{d}}$, and $\ddot{\mathbf{d}} \in \mathbb{R}^{n^d}$ denote displacement, velocity, and acceleration responses. As described in Table 2 the external load in the initial state $\mathbf{p}^0$ (i.e. before the train enters the bridge) contains a prestress load applied through actuation $\mathbf{p}^{ps} = \mathbf{D}\Delta\mathbf{l}^{ps}$. Train $\mathbf{p}^t(t)$ and actuation load $\mathbf{p}^{act}(t)$ are time dependent.

The actuation load $\mathbf{p}^{act}(t)$ models the effect of the actuator length changes $\Delta\mathbf{l}$. The actuator action is treated as equivalent external load:

$$\mathbf{p}^{act}(t) = \mathbf{D}\Delta\mathbf{l}(t) \tag{2}$$

where the input matrix $\mathbf{D} \in \mathbb{R}^{n^d \times n^{act}}$ collates column-wise the equivalent loads causing a unitary length change of the actuator housing elements:

$$\mathbf{D} = \begin{bmatrix} \boldsymbol{\delta}_1 & \boldsymbol{\delta}_2 & \dots & \boldsymbol{\delta}_{n_{act}} \end{bmatrix}, \ \overline{\boldsymbol{\delta}}_i = \overline{\mathbf{T}}_i^T \begin{bmatrix} -\frac{E_i A_i}{l_i} & 0 & 0 & \frac{E_i A_i}{l_i} & 0 & 0 \end{bmatrix}^T \tag{3}$$

For simplicity, the notation for time dependent '(t)' is omitted hereafter. The vector $\boldsymbol{\delta}_i \in \mathbb{R}^{n^d}$ is constructed by assembling the components of $\overline{\boldsymbol{\delta}}_i \in \mathbb{R}^6$ into the corresponding global degrees of freedom. E_i, A_i, and l_i denote the Young's modulus, cross-sectional area, and length of the i-th actuator housing element, and $\overline{\mathbf{T}}_i \in \mathbb{R}^{6\times6}$ is the local-to-global transformation matrix for 2D beam elements. The vector $\mathbf{p}^{act}$ therefore represents the equivalent nodal forces that, when applied to the structure, reproduce the same deformation state as that induced by actuator elongations $\Delta\mathbf{l}$. Note that active strut length variations result from inelastic length changes of the actuators. For simplicity, equivalent external loads are employed to model the effect of such changes, which is correct for defining the deformation state.

However, the force produced in the housing element must be computed by eliminating the inelastic part from the total strain of the element. Accordingly, the internal force vector in each housing element $\mathbf{f}_i^c \in \mathbb{R}^6$ is obtained as:

$$\mathbf{f}_i^c = \begin{cases} \overline{\mathbf{K}}_i \ \overline{\mathbf{T}}_i \ \overline{\mathbf{d}}_i^c - \overline{\mathbf{T}}_i^T \begin{bmatrix} -\frac{E_i A_i}{l_i} & 0 & 0 & \frac{E_i A_i}{l_i} & 0 & 0 \end{bmatrix}^T \Delta l_i, & \text{if } i \in S^{act}, \\ \overline{\mathbf{K}}_i \ \overline{\mathbf{T}}_i \ \overline{\mathbf{d}}_i^c, & \text{otherwise.} \end{cases} \tag{4}$$

where $\overline{\mathbf{K}}_i \in \mathbb{R}^{6\times6}$ is the stiffness matrix of the i-th element, $\overline{\mathbf{d}}_i^c \in \mathbb{R}^6$ the displacement vector, and S^{act} the set of actuator housing elements. The matrix $\overline{\mathbf{K}}_i \in \mathbb{R}^{6\times6}$ denotes the stiffness matrix of the i-th element, and the vector $\overline{\mathbf{d}}_i^c \in \mathbb{R}^6$ represents the corresponding element displacement vector, containing the six components of $\mathbf{d}^c \in \mathbb{R}^{n^d}$ associated with the degrees of freedom of the i-th element.

The steady state is derived using the state-space formulation:

$$\dot{\mathbf{z}} = \mathbf{A}\mathbf{z} + \mathbf{B}\Delta\mathbf{l} + \mathbf{H}\mathbf{p}^t \tag{5}$$

$$\mathbf{A} = \begin{bmatrix} \mathbf{0} & \mathbf{I} \\ -\mathbf{M}^{-1}\mathbf{K} & -\mathbf{M}^{-1}\mathbf{C} \end{bmatrix}, \quad \mathbf{B} = \begin{bmatrix} \mathbf{0} \\ \mathbf{M}^{-1}\mathbf{D} \end{bmatrix}, \quad \mathbf{H} = \begin{bmatrix} \mathbf{I} \\ \mathbf{M}^{-1} \end{bmatrix} \tag{6}$$

The state vector $\mathbf{z}(t) \in \mathbb{R}^{2n^d}$ collates displacement and velocity responses:

$$\mathbf{z} = \begin{bmatrix} \mathbf{d}^c \\ \dot{\mathbf{d}}^c \end{bmatrix} \tag{7}$$

The control inputs, i.e. the actuator length changes, are computed using a Linear Quadratic Regulator (LQR):

$$J = \frac{1}{2}\int_0^\infty \left(\mathbf{z}^T\mathbf{Q}\mathbf{z} + \Delta\mathbf{l}^T\mathbf{R}\Delta\mathbf{l}\right)\, dt \tag{8}$$

The LQR formulation is based on the minimisation of the performance index of $\mathbf{J}$ that quantifies the energy associated with the closed-loop system. The weighting matrices $\mathbf{Q} \in \mathbb{R}^{2n^d \times 2n^d}$ and $\mathbf{R} \in \mathbb{R}^{n^{act} \times n^{act}}$ are set to achieve a balance between response reduction and control effort. In this work, the coefficients are calibrated to ensure that the uncontrolled peak displacement is reduced below the serviceability limit state (SLS) through actuator length adjustments of less than 100 mm. The reader is referred to Reksowardojo et al. (2024b) for further formulation details.

3.7. Control-force transfer and stress-constrained 2D–3D matching

The control input used in the reduced-order 2D analysis and subsequently applied to the high-fidelity 3D finite-element model is obtained through an iterative matching procedure between the two systems. The purpose of this procedure is to transfer the actuator force history derived from the 2D control analysis to the 3D model, while ensuring that both global and local stress limits are satisfied throughout the design process. To enable consistent force transfer, the fundamental frequencies of the 2D and 3D models are aligned. This allows the actuator force to retain the same temporal waveform in both analyses, ensuring that the imposed signal accurately reproduces the critical train velocity associated with resonance behaviour.

Let $\mathbf{p}^{act}(t)$ denote the actuator force history obtained from the 2D control analysis, and let $\mathbf{p}^{act*}(t)$ denote its adjusted version applied to the 3D model. The corresponding structural response of the 3D system is expressed as:

$$\mathbf{r}_{3D}(t) = \mathbf{r}_{3D}\left(\mathbf{p}^{act*}(t)\right) \tag{9}$$

where $\mathbf{r}(t)$ denotes the structural response and the subscript indicates the dimensionality of the model. In this study, the governing limit state is stress-based; therefore, the response quantity used for matching is the stress response.

The adjustment of the actuator force history is formulated as a min–max problem to ensure that stress-based ultimate limit state requirements are satisfied at all time instants during the loading event. Since both the actuator input and the resulting structural response are time-dependent, the

governing condition is dictated by the maximum stress excursion over time rather than by an average or integrated measure. Accordingly, the residual stress margin is defined as:

$$\mathbf{\Delta r}(t) = \mathbf{r}_{ULS} - \mathbf{r}_{3D}(t) \tag{10}$$

where $\mathbf{r}_{3D}(t)$ is the stress response of the 3D model induced by the adjusted actuator force history and $\mathbf{r}_{ULS}$ denotes the admissible stress limit. The adjusted actuator force $\mathbf{p}^{act*}(t)$ is obtained by solving the following min–max problem:

$$\begin{aligned} &\min_{\mathbf{p}^{act*}(t)} \quad \min_{t\in[0,\,T]} |\mathbf{\Delta r}(t)| \\ &\text{s.t.} \qquad \mathbf{\Delta r}(t) \geq 0 \quad \forall t \in [0, T] \end{aligned} \tag{11}$$

where $[0, T]$ denotes the duration of the simulated loading event. This formulation enforces the stress constraint uniformly over time, such that the actuator force is adjusted to prevent exceedance of the stress limit at the most critical instant. In practice, this min–max statement represents an iterative matching and verification procedure rather than a formally solved continuous optimisation problem. It reflects the design intent that the actuator force history transferred from the 2D control model must remain admissible in the 3D model under the worst-case stress demand during the entire loading cycle.

4. Bridge response under external and actuation loads

4.1. Structural design

The structural components of the box girder are fabricated from S355 structural steel. The geometry is defined by a girder depth of 2,000 mm, an upper flange width of 4,700 mm, and a lower flange width of 2,400 mm. The upper flange is designed as a composite section comprising a 300 mm reinforced concrete layer bonded to an 18 mm steel plate, providing increased stiffness and load-carrying capacity. The bottom flange and web plates have a uniform thickness of 18 mm, consistent with the diaphragm plates, which are also 18 mm thick. A diaphragm cut-out with an in-plane dimension of 500 mm is included. Structural stiffening is provided by longitudinal stiffeners with a height of 150 mm and a thickness of 10 mm. Connection detailing is realised through welded joints with a specified throat thickness of 8 mm. The welded joints are modelled with S355 base steel and a weld consumable with a minimum ultimate tensile strength of approximately 490 MPa, corresponding to AWS E7018 or EN ISO 2560-A E 42 class electrodes, in accordance with standard bridge fabrication practice.

The mechanical structure of the EAT system consists of a capping beam, struts, and a steel cable. The capping beam is composed of S355 structural steel and is designed with an HEB 200 cross section. Stiffeners with a thickness of 10 mm are integrated into the beam configuration. The strut members are also manufactured from S355 steel and are specified with a rectangular hollow section (RHS) of 120 mm edge length and a wall thickness of 12 mm. The employed steel cable has a nominal diameter of 110 mm. Table 3 provides detailed specifications for the box girder and the EAT system, including material properties, geometric parameters, and load-carrying capacities. These specifications have been verified in accordance with Eurocode 3 (CEN, 2005a), confirming that the structure satisfies Ultimate Limit State (ULS) requirements without the need for active control. The Fatigue Limit State (FLS) is addressed in subsequent sections, focusing on damage accumulation and service life estimation under repeated loading.

Table 3. Technical specifications box-girder and EAT system.

Box-girder	
Material specification	S355
Overall dimension	Height: 2,000 mm Upper plate width: 4,700 mm Lower plate width: 2,400 mm
Upper plate	Composite layup: Concrete layer: 300 mm Steel layer: 18 mm
Bottom plate and side plate	Thickness: 18 mm
Diaphragm	Thickness: 18 mm Cut-out in-plane thickness: 500 mm
Stiffener	Height: 150 mm Thickness: 10 mm
Welding	Throat thickness: 8 mm AWS E7018 (UTS ≈ 490 MPa) or EN ISO 2560-A E 42
EAT system	
Capping beam	Material: S355 Cross section: HEB 200 Stiffener thickness: 10 mm
Strut	Material: S355 Cross section: RHS – Diameter 120 × 12 mm
Cable	Diameter: 110 mm

4.2. Dynamic characteristics

The critical velocity v inducing resonance is related to the bridge eigenfrequencies as per (Y.-B. Yang et al., 1997):

$$\frac{v}{s} \approx \frac{\omega_k}{2\pi} \quad \forall k = \{1, 2, 3, \ldots\} \tag{12}$$

where s is the train axle spacing and ω_k the k^{th} eigenfrequency. For simplicity, the train axles are assumed to be regularly spaced, with a spacing equal to the train car length l^w. For the T2 train load applied to the non-retrofitted bridge, the critical velocity that induces resonance with the first eigenfrequency is calculated as $v = 67.64$ m s^{-1}. As also observed by Reksowardojo et al. (2024b), excitation at this velocity predominantly activates the first vibration mode. Accordingly, the present study focuses on this most critical resonance scenario associated with the T2 train type travelling at the critical velocity.

To ensure consistency between the reduced-order 2D model and the high-fidelity 3D model, their dynamic behaviour is calibrated by aligning eigenfrequencies and associated mode shapes. Figure 8 compares the fundamental frequency obtained from the 2D and 3D models. The first mode exhibits negligible discrepancy, indicating good agreement in the global dynamic response. In contrast, higher modes show increasing differences due to the higher modelling fidelity of the 3D model, particularly the explicit representation of diaphragms and local structural features that

primarily affect higher-order modal behaviour. For the purposes of this study, such discrepancies are not critical. Since resonance under moving train loads is governed by the fundamental frequency and the associated global mode shape, accurate alignment of the first mode is sufficient to reproduce the dominant dynamic response and to carry out the subsequent fatigue damage assessment.

4.3. Actuator force input

Figure 9 shows the actuation force for the 2D model, presented in both frequency and time domains. The frequency-domain analysis highlights the dominant excitation frequency, primarily associated with the first mode, guiding the required control effort. This actuator force profile is then applied to the 3D model, with iterative adjustments ensuring compatibility with the higher-fidelity configuration as described in 3.7.

4.4. Stress response

4.4.1. Global response

Regarding the stress response obtained from the 3D model, there is generally good agreement with the results of the 2D analysis. The primary differences arise from shear lag effects at the intersections of webs and diaphragms, which are inherently captured in the 3D representation. These effects lead to a more nuanced stress distribution across the cross-section, as illustrated in Figure 10.

Figure 10 illustrates the global reduction in von Mises stress, shown here for visualisation purposes. All fatigue verifications are performed using principal stress histories

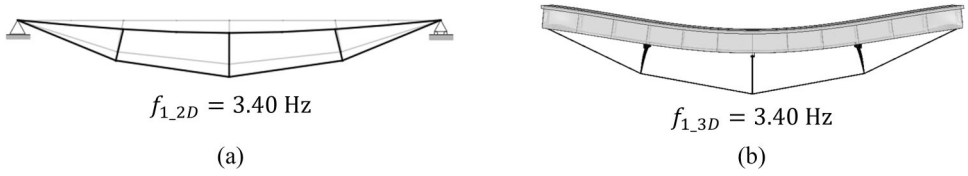

Figure 8. Fundamental frequency match (a) 2D, and (b) 3D analysis.

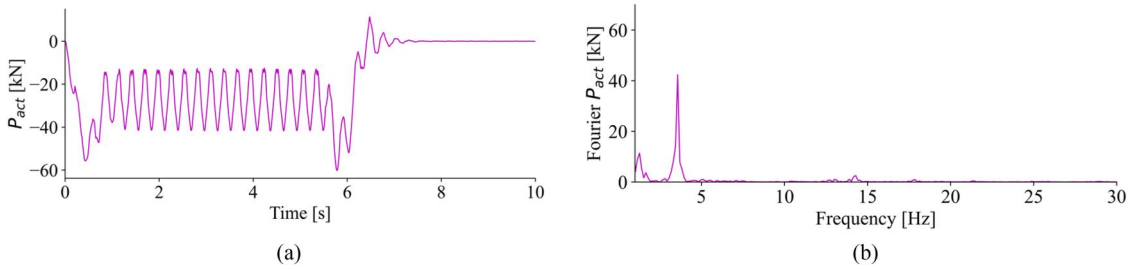

Figure 9. Actuation force input in time (a) and frequency (b) domains.

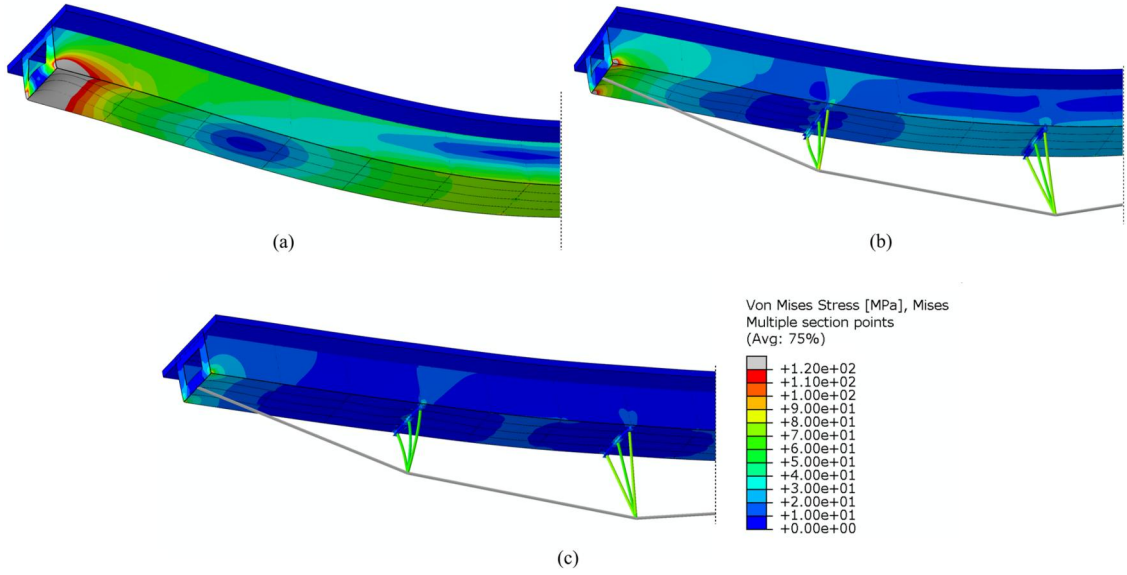

Figure 10. Von Mises stress distribution in the steel box girder deck, $t = 5$ s (deformation scale 1:150): (a) before retrofit; (b) with External Passive Tensioning (EPT); (c) with External Adaptive Tensioning (EAT).

extracted at welded details, consistent with Eurocode 3 (CEN, 2005b), whereas the von Mises field is used solely to illustrate overall stress redistribution under adaptive control. The stress distribution analysis reveals a significant reduction in stress within the steel deck due to the implementation of retrofitting systems. The EPT system achieves a stress reduction of approximately 40% relative to the un-retrofitted configuration (case d vs. case b in Table 2). The EAT system further improves performance, yielding a stress reduction of 66% compared to the same baseline (case f vs. case b). When comparing the two retrofitting strategies directly, the EAT system reduces stress by approximately 43% relative to the EPT system (case f vs. case d), demonstrating its superior effectiveness.

4.4.2. Capping beam and active strut interface

The capping beam is designed to effectively transfer actuator forces to the box girder while avoiding unintended stress concentrations. Its performance is verified for both Ultimate Limit State (ULS) and Fatigue Limit State (FLS) in accordance with Eurocode 3 (CEN, 2005a), ensuring structural integrity under extreme and cyclic loading. An HEB 200 section is selected for its balance of structural efficiency and practicality, with a 10 mm stiffener thickness to enhance fatigue resistance and load-bearing capacity. Figure 11 illustrates the von Mises stress distribution in the capping beam resulting from the force transmitted by the active struts.

Figure 12 illustrates the stress response at the critical location governing the Ultimate Limit State (ULS) design of the capping beam–strut connection. The analysis yields a maximum equivalent (von Mises) stress of 297 MPa, which remains below the yield strength of S355 steel. This confirms that the structural response remains within the elastic regime under ULS loading conditions. As no plastic deformation is observed, the integrity of the capping beam–strut connection is preserved, and the design complies with strength and serviceability requirements.

5. Damage assessment

5.1. Damage scenarios

The primary objective of this study is to evaluate the effectiveness of the EAT system in mitigating fatigue-induced

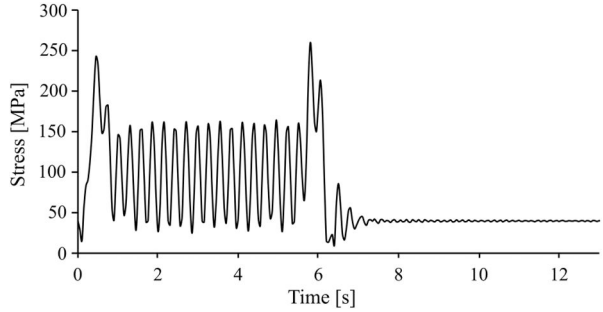

Figure 12. Stress response at the critical location along the interface between the actuator housing and the box-girder bottom flange.

deterioration in railway bridge structures. The principal metric adopted for this assessment is the Remaining Useful Life (RUL), defined as the number of additional train passages the bridge can sustain before cumulative fatigue damage exceeds allowable thresholds at one or more critical locations. Fatigue accumulation results from repeated load cycles, with each train passage contributing to damage through quasi-static effects associated with the train's weight and, more critically, through dynamic excitations induced by vibrations. The RUL metric serves as a predictive indicator of the structure's residual capacity under continued operational loading.

When the EAT system is integrated at the construction stage, its influence extends over the entire design life of the bridge, potentially optimising long-term performance and delaying the onset of fatigue-critical conditions. Conversely, if the system is deployed as a retrofit intervention, its impact is confined to prolonging the structure's remaining service life from the point of installation onward, without altering the cumulative fatigue accrued prior to activation. To evaluate the effectiveness of the EAT system, this study compares three configurations:

- The initial condition prior to the implementation of any retrofitting measures (NR). This configuration serves as the baseline assessment of fatigue accumulation without retrofit-induced stiffness enhancements and corresponds to case b in Table 2.
- The bridge retrofitted with an External Passive Tensioning (EPT) system, which provides the same prestressed state as the EAT system but lacks dynamic adaptability to loading

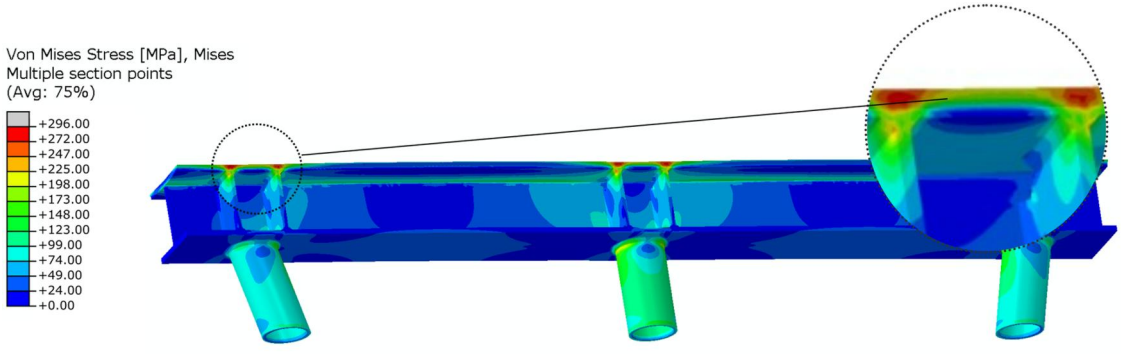

Figure 11. Local stress peak induced by the punching force at the strut–capping beam interface.

variations. The implementation of this retrofitting measure results in cases d and e in Table 2.
- The bridge retrofitted with an External Adaptive Tensioning (EAT) system (case f in Table 2).

The benchmark between EAT and NR evaluates the added value of EAT in comparison to the non-retrofitted configuration. However, an equally important consideration is whether the additional investment in an active system is justified and under what conditions it becomes economically and structurally viable. To address this, a comparison with an External Passive Tensioning (EPT) system is included. An EAT system is a mechatronic solution consisting of sensors, actuators, control mechanisms, power supply, and signal transmission components. Due to variations in design complexity, component reliability, maintenance schedules, and operational conditions, the system may experience periods of reduced functionality or downtime. The implications of a non-operational EAT system on bridge performance and fatigue damage must be clearly defined. To evaluate these effects, two EAT system failure scenarios are considered: EAT-NO1 and EAT-NO2.

5.1.1. EAT-NO1: partial loss of active functionality

In this failure variant, the EAT system becomes non-operational, leading to the loss of active tensioning and damping capabilities. However, the initial pre-tensioning remains intact, allowing the bridge to function similarly to an EPT system. Under these conditions, the bridge behaviour aligns with cases d and e in Table 2. From a technical perspective, this scenario requires the EAT system to be designed so that pre-tensioning remains effective even in the event of active component failure. This can be achieved mechanically by pre-tensioning the system when actuators are positioned at their end limits. In case of failure:

- All actuators are locked, ensuring that the pre-tensioning remains stable.
- Alternative safety mechanisms may be required, such as actuator safeguarding systems or safety locking devices for the adjustment mechanisms.

If maintenance activities involve the replacement of load-bearing components and cannot be performed between two train passages, an alternative load path must be established during maintenance to maintain structural stability.

5.1.2. EAT-NO2: complete loss of functionality

In this failure variant, the EAT system becomes entirely non-operational, resulting in a complete loss of both tensioning and damping functions. This scenario is equivalent to a non-retrofitted bridge, where the structure operates as if no active or passive system were ever installed. Consequently, the bridge behaviour corresponds to case b in Table 2. This scenario highlights the importance of redundancy and fail-safe mechanisms in the design of mechatronic structural enhancement systems, ensuring that failure conditions do not lead to unexpected stress accumulation or excessive fatigue deterioration.

5.1.3. Active System Utilisation

To systematically account for operational variances, the concept of Active System Utilisation (ASU) is introduced as a key performance indicator, quantifying the proportion of train passages during which the EAT system remains fully operational:

- 100% ASU: The EAT system is functional during every train passage, providing maximum fatigue mitigation.
- 0% ASU: The EAT system remains in constant downtime reducing performance to a passive (EAT-NO1) or non-retrofitted state (EAT-NO2).

ASU is defined as the average availability of the EAT system during train passages over the interval $[N^{crs}, N^{cre}]$ and is expressed as:

$$ASU = \frac{1}{N^{cre} - N^{crs}} \sum_{N^{cr}=N^{crs}}^{N^{cre}} ASU(N^{cr}) \tag{13}$$

where N^{cr} denotes the train-passage index, N^{crs} the first passage after implementation of the EAT system, and N^{cre} the passage at which the cumulative fatigue damage threshold is exceeded, marking the end of service life. Each train passage includes both the actual crossing and the subsequent oscillation phase of the bridge. Equation (13) extends Ebeling's formulation of interval availability (Ebeling, 2019) to a passage-based framework. In this discrete representation, each train passage is treated as a single event during which the availability of the EAT system remains constant. Consequently, ASU varies between successive passages rather than within an individual passage. This formulation reflects the operational nature of the metric while remaining consistent with Ebeling's concept of average interval availability. ASU quantifies the fraction of train passages during which the EAT system is operational after installation. It is used as a parametric indicator linking the system's functional availability to the bridge's fatigue performance, rather than as a full probabilistic model of component reliability (actuators, sensors, power supply, control units, and software). This representation of EAT system availability is distinct from the structural fatigue behaviour of the bridge itself, which is evaluated through cumulative damage analysis in accordance with Eurocode 3 (CEN, 2005b), using ASU as an input parameter to account for system downtime effects.

By incorporating Active System Utilisation (ASU) into fatigue analysis, the impact of system failures and maintenance-related downtimes can be better predicted. The range of operational scenarios, from full functionality (100% ASU) to complete failure (0% ASU), allows for a realistic evaluation of how EAT retrofitting influences the long-term performance and service life of the bridge. These insights contribute to life-cycle assessments, ensuring that design strategies and maintenance plans are robust enough to

maintain structural integrity and minimise fatigue-related failures over time. Both EAT-NO1 and EAT-NO2 are classified as non-safety-critical failure scenarios, as neither compromises the structural stability of the bridge. Additionally, the fatigue damage induced by train passages in these failure states does not exceed the levels observed in the non-retrofitted (NR) condition. However, the implementation of EAT-NO1 may require greater technical effort compared to EAT-NO2, as it necessitates mechanisms that maintain pretensioning despite the failure of active components. This includes locking mechanisms or safeguard systems to ensure structural performance is preserved in the absence of active control. The decision between EAT-NO1 and EAT-NO2 should be made on a case-by-case basis, considering the trade-off between implementation effort and expected benefits (see Section 5.3).

5.2. Damage assessment

5.2.1. Methodology

In fatigue assessment, lifetime models estimate the service life of structural components under cyclic loading by integrating variable-amplitude load characterisation, fatigue resistance, and cumulative damage evaluation. Load spectra derived from operational data are processed using rainflow counting to extract representative stress cycles, which are evaluated against material S-N curves while accounting for geometric effects such as weld-induced stress concentrations. Cumulative damage is typically assessed using linear models such as Palmgren-Miner, with fatigue failure assumed upon reaching a critical damage threshold. The choice of verification method, nominal stress or local approaches, is critical for accurately capturing stress amplification due to geometric and weld-related discontinuities.

For bridge structures under repeated train loading, individual fatigue models are assigned to critical locations. These models estimate the number of cycles to failure and track damage accumulation to compute the Remaining Useful Life (RUL). The analysis point reaching the critical damage threshold first defines the system-level RUL, enabling a reliability-based assessment of structural integrity under continued service conditions. For scenarios involving the EAT system, damage evaluation incorporates proportional weighting based on the Active System Utilisation (ASU) and the assumed failure mode EAT-NO1 or EAT-NO2:

- EAT-NO1: Damage at each analysis point is computed by proportionally combining results from the EAT and EPT scenarios, representing partial degradation of active control.
- EAT-NO2: Damage integrates outcomes from the EAT and NR cases, simulating a complete loss of both active and passive tensioning effects.

This methodology captures variability in system performance and downtime, ensuring accurate Remaining Useful Life (RUL) estimation under degraded conditions. The maximum damage across all inspection points defines the critical location and governs the RUL for each scenario. This comparative framework enables a robust assessment of how adaptive (EAT) and passive (EPT) tensioning strategies influence fatigue life and structural reliability.

5.2.2. Critical points and damage accumulation

The methodology for fatigue damage quantification follows a structured sequence aimed at accurately predicting component lifespan under cyclic loading. The process begins with the identification of potentially critical regions where fatigue failure is most likely to occur. These include locations characterised by stress concentrations, geometric discontinuities, and welded joints, as well as regions subjected to high stress amplitudes or frequent stress fluctuations. The final selection of critical locations is based on a combined assessment of stress magnitude and loading variability, ensuring that detailed fatigue analyses are concentrated on the most fatigue-vulnerable components.

For the bridge under investigation, given the prevalence of tensile stresses, the underside of the box girder is prioritised as the primary area of concern. Two categories of locations are examined in detail:

- Mid-span region: in the non-retrofitted (NR) configuration, peak tensile stresses occur at mid-span due to excitation of the fundamental vibration mode.
- Actuator-free regions: when actuator forces are applied, the stress field is redistributed; however, areas not directly affected by these forces, particularly near stiffness discontinuities, may still accumulate fatigue damage. These actuator-free zones, are therefore included in the analysis to ensure a comprehensive assessment of fatigue performance across the structure.

Three specific locations are analysed within each selected region, which are illustrated in Figure 13:

- Diaphragm Cut-out Edge: located along the upper edge of the diaphragm, this area features abrupt stiffness discontinuities introduced by cut-outs, making it a likely hotspot for stress concentration.
- Diaphragm-to-Side/Bottom Plate Transition: this location includes the connection between the diaphragm and the side plate, as well as the transition to the bottom plate. Both interfaces are prone to complex stress states due to geometry and load redistribution.
- Diaphragm-to-Longitudinal Stiffener Transition: this region encompasses the connections between the diaphragm and the longitudinal stiffener, the diaphragm and the bottom plate, and the longitudinal stiffener and the bottom plate. These intersecting interfaces are structurally critical and require detailed analysis for fatigue assessment under dynamic loading.

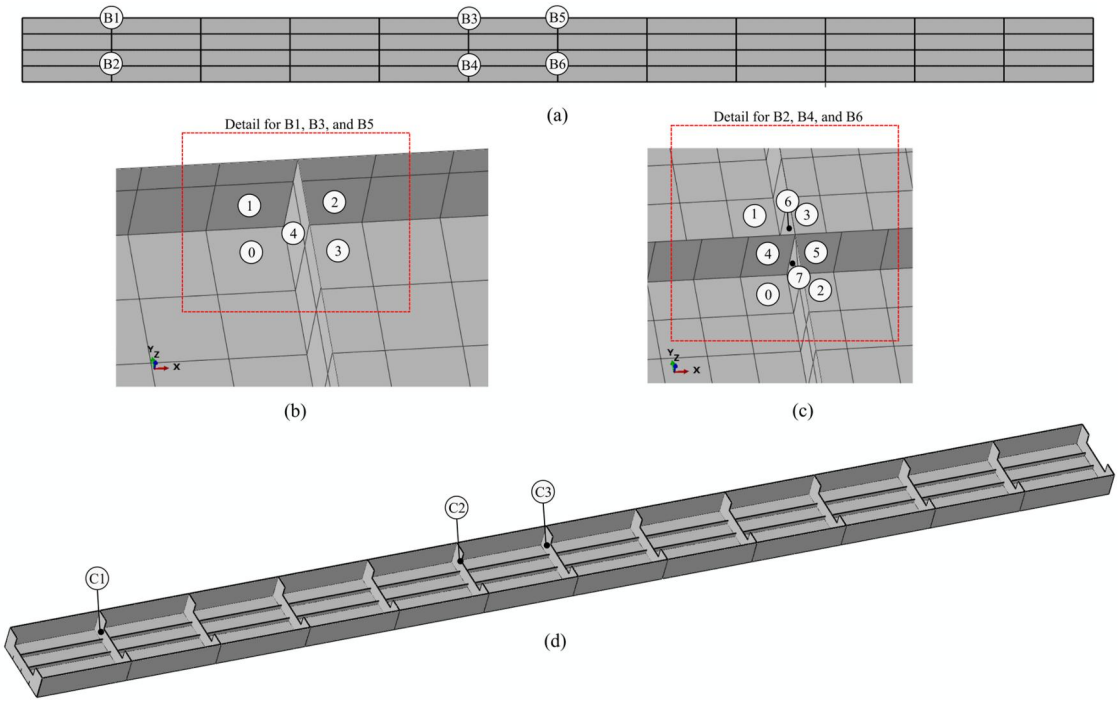

Figure 13. Critical stress location: (a) areas B1, B2, B3, B4, B5, B6; (b) area B1, B3, and B5 critical point detail; (c) area B2, B4, and B6 critical point detail; (d) diaphragm C1, C2, C3.

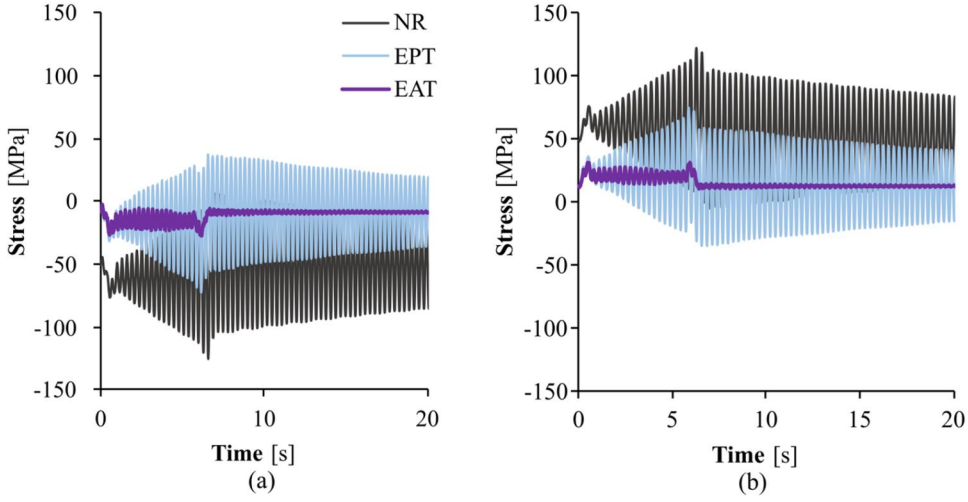

Figure 14. Stress fluctuation of normal stress longitudinal to the bridge in: (a) B1 and (b) B5.

For all areas labelled as 'B', a detailed examination of the heat-affected zones (HAZ) at weld seam terminations is conducted to assess localised fatigue risks.

Figure 14 presents the longitudinal normal stress response at locations B1 and B5 over the first 20 s following train entry onto the bridge. Stress histories at the identified critical points cover a 98-second period, including approximately 7 s of active train loading followed by 90 s of free vibration to allow the structure to return to a stationary state. Unlike global analyses that provide a macro-scale view, these localised stress histories are extracted directly at critical locations, capturing both the amplitude and temporal evolution of fluctuations induced by train passages and offering detailed insight into fatigue-relevant loading. As expected, the EPT system moderately reduces stresses compared to the non-retrofitted (NR) case, with only slight effects on peak amplitudes and vibration decay. By contrast, the EAT system achieves a substantial stress reduction and significantly faster damping, highlighting its superior capability to mitigate fatigue-critical stresses and improve dynamic performance.

For fatigue verification in line with Eurocode 3 (CEN, 2005b), the stress components are transformed into principal stresses, enabling a damage-focused evaluation by isolating the most critical tensile stresses that drive crack initiation. This transformation also ensures coordinate-independent assessment under multiaxial stress states typical of welded joints and complex geometries. The rainflow counting method is then applied to these principal stress histories, decomposing irregular time signals into discrete load cycles to classify amplitudes, mean values, and frequencies, thus forming the load spectra for

cumulative damage analysis. For example, Figure 15 shows the principal stress cycles and corresponding amplitude history at area B2, point 5 under the EPT scenario.

Fatigue life at each critical detail is evaluated using S-N curves in accordance with Eurocode 3 (CEN, 2005b), ensuring alignment with the appropriate detail category (e.g. welded joints, notches). These curves relate stress amplitude to the number of cycles to failure and form the basis for cumulative damage assessment. Fatigue strength (FAT) classes are assigned to standardised structural details, particularly welded joints, based on factors such as weld type (e.g. fillet, butt), connection geometry, and loading direction. Each FAT class corresponds to a specific S-N curve, which is integrated into the fatigue life model. Figure 16 presents the three key structural details identified in this study, along with their associated S-N curves:

- the longitudinal weld seam joining the bottom and side plates (splice),
- the heat-affected zones (HAZs) at welds connecting plates and flanges of built-up sections on the bottom plates,
- the HAZ at the stiffener-to-diaphragm transition.

These details are highlighted due to their criticality in the subsequent fatigue analysis. All relevant locations described in Section 5.2.2 are also evaluated using the corresponding FAT classes.

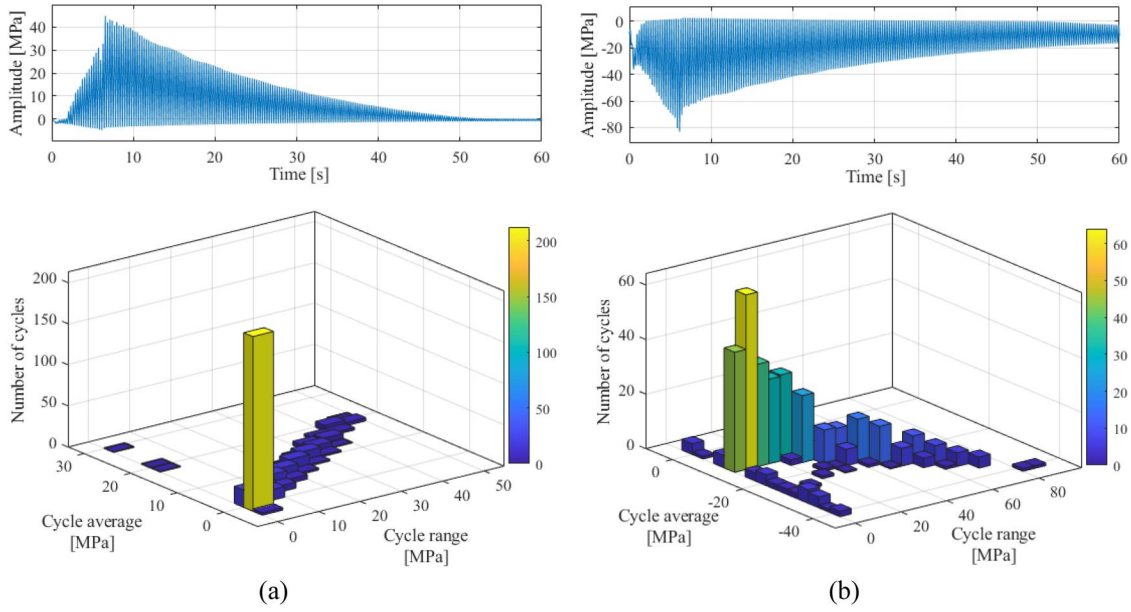

Figure 15. Rainflow analysis in area B2 point 5: (a) principal stress σ_1 and (b) principal stress σ_2.

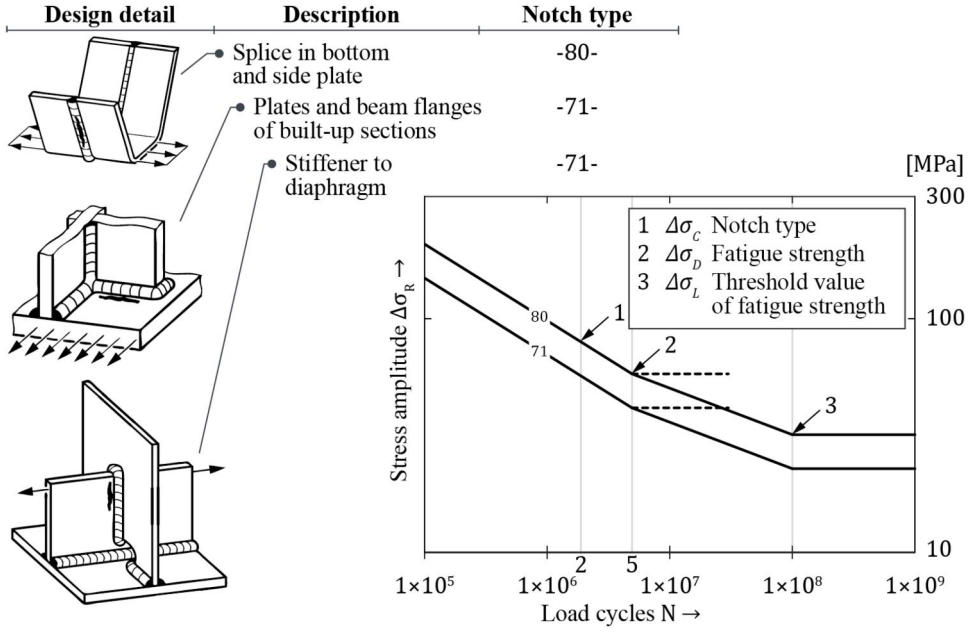

Figure 16. Design details used to define notch types and corresponding S–N curves for welded structural elements exhibiting sharp notch effects (based on Eurocode 3 (CEN, 2005b)).

The interaction between loading and structural capacity is established by mapping the extracted load spectrum onto the fatigue life framework, forming the basis for cumulative damage assessment. This process follows the linear damage accumulation hypothesis, typically represented by Palmgren-Miner's rule. Each stress magnitude identified in the spectrum is associated with a fatigue life value N_i from the appropriate S–N curve, in accordance with Eurocode 3 (CEN, 2005b). The corresponding number of cycles n_i is used to compute the damage contribution $u_i = \frac{n_i}{N_i}$. Total fatigue damage is then expressed as:

$$U = \sum u_i = \sum \frac{n_i}{N_i} \tag{14}$$

This cumulative damage is evaluated per train passage to quantify fatigue progression at critical locations. A damage sum $U \geq 1$ indicates potential fatigue failure, signifying that the accumulated loading has reached the structural fatigue limit. This approach ensures fatigue life predictions are consistently based on material properties, stress histories, and actual loading conditions.

Following Eurocode 3 (CEN, 2005b), compressive stress ranges are treated equivalently to tensile ranges for welded details without stress relief annealing, and no mean stress correction is applied. Consequently, only the stress magnitudes obtained from rainflow counting are used in the fatigue assessment. This simplifies the damage evaluation process, as contributions can be calculated directly from the principal stress ranges using a cumulative damage model, without additional stress classification. For each critical detail, total fatigue damage is computed by summing the individual contributions from all principal stress cycles, providing an accurate representation of fatigue accumulation at sensitive structural locations.

5.3. Remaining useful life (RUL) benchmark

5.3.1. NR vs EPT vs EAT

For each configuration non-retrofitted (NR), EPT, and EAT the most critical points are identified and analysed. Since the effectiveness of EPT and EAT depends on the timing of their application (see Section 5.1), the analysis uses a relative reference to the Remaining Useful Life (RUL) of the NR case, computed individually for each point. The relative damage ratio compares the damage under EPT or EAT to that of the NR configuration. A ratio below 100% indicates reduced damage, whereas a value above 100% implies increased fatigue accumulation. The corresponding RUL for EPT or EAT is derived by multiplying the NR-based RUL by the inverse of the damage ratio. System-level fatigue life is governed by the first critical point to reach a damage sum of $U \geq 1$. Table 4 summarises the key critical points, reporting damage per train passage for each configuration, along with the damage ratios EPT/NR and EAT/NR. These ratios provide a direct estimate of the lifetime extension potential relative to the NR case. While operational energy demands and maintenance requirements of the EAT system are disregarded here, the damage ratios can serve as a basis for a simplified cost-benefit comparison.

Among all configurations, area B2, point 5 remains the most critical location. The EPT system reduces damage at B2 point 5 to 17.2% of the NR case, corresponding to a theoretical RUL extension by a factor of approximately 5.8. Notably, EPT causes a substantial increase in damage at B1 point 4 (>25,000%), but this location is not life-limiting due to its low absolute damage level. This highlights the importance of evaluating all critical points across configurations rather than focusing solely on those critical in the NR case. In contrast, the EAT system fully mitigates fatigue damage from train passages at all critical locations under the examined conditions, indicating its superior performance in preserving structural integrity.

5.3.2. Sensitivity to FAT class variation

To evaluate the robustness of the fatigue assessment against uncertainties in weld classifications, a sensitivity analysis was conducted by varying the assigned FAT class by ± 1 category. This variation corresponds to approximately ±12% change in allowable stress range per Eurocode 3 (CEN, 2005b). Table 5 presents results for the critical point 5 in area B2. The cumulative damage variation remains marginal across all cases and does not alter the relative performance ranking among configurations. The EAT case consistently demonstrates negligible fatigue damage across all FAT class variations. Damage per train passage in the NR case responds non-linearly to FAT class changes: decreasing the FAT class increases damage by 44.2%, while increasing it reduces damage by 31.8%.

Consequently, EAT's effectiveness in extending structural lifetime becomes more pronounced with lower FAT classes, as the baseline damage reduction potential increases. In contrast, EPT exhibits reduced effectiveness at lower FAT classes. This suggests that EPT requires the structure to retain a minimum strength threshold to achieve meaningful

Table 4. Summary of the most critical fatigue-prone locations for the NR, EPT, and EAT configurations.

	Damage per train passage	Damage ratio	
Description of critical point	NR	EPT/NR	EAT/NR
Area B1 point 4	1.51×10^{-8}	250-fold increase	~0%
Area B2 point 4	7.91×10^{-5}	15.7%	~0%
Area B2 point 5	1.19×10^{-4}	17.2%	~0%
Area B4 point 4	4.55×10^{-5}	23.1%	~0%
Area B4 point 5	4.41×10^{-5}	23.8%	~0%
Area B6 point 4	5.86×10^{-5}	10.6%	~0%
Area B6 point 5	5.87×10^{-5}	10.5%	~0%

Table 5. Effect of FAT class variation on cumulative damage at critical point 5 in area B2.

	Damage per train passage NR		Damage ratio	
Critical point: area B2 point 5	Absolute	Relative to FAT	EPT/NR	EAT/NR
FAT+1	0.83×10^{-4}	69.2%	15.6%	∼0%
FAT	1.19×10^{-4}	100.0%	17.2%	∼0%
FAT-1	1.72×10^{-4}	144.2%	18.5%	∼0%

benefits. These findings confirm that fatigue-life predictions remain robust despite reasonable uncertainties in FAT class selection, with the observed variations insufficient to change the fundamental performance hierarchy of the analysed configurations.

5.3.3. RUL with active system utilisation

This section evaluates the Remaining Useful Life (RUL) of the bridge in terms of allowable train passages, accounting for both the individual performance of the three dynamic configurations (NR, EPT, EAT), as previously analysed, and the impact of EAT system downtime, introduced in Section 5.1. Such downtime may result from actuator failures, control system malfunctions, or sensor issues. Depending on the failure type, the system may either:

- Operate an External Passive Tensioning (EPT) system (EAT-NO1).
- Cease to provide support entirely, reverting to the non-retrofitted condition (EAT-NO2).

As defined in 5.1, ASU is the proportion of train passages during which the EAT system is fully operational and actively engaged in load mitigation. The complementary proportion, i.e. 1 − ASU represents the EAT system downtime, during which the system is non-functional due to actuator failures, control issues, sensor malfunctions or scheduled maintenance. This operational definition of ASU is consistent with the concept of interval availability as defined by Ebeling (Ebeling, 2019). Figure 17 illustrates the relationship between ASU and the bridge's RUL under varying levels of EAT system downtime. The EAT-NO1 and EAT-NO2 configurations therefore represent practical realisations of fail-safe behaviour during periods when the active system is unavailable. The analysis references two baseline conditions:

a. NR baseline: no EAT or EPT system is present.
b. EPT baseline: a passive tensioning system (EPT) is in place throughout the bridge's service life.

In both plots, the horizontal axis shows ASU, and the vertical axis indicates the RUL relative to the selected baseline, plotted on a logarithmic scale. The results quantify how decreasing ASU, i.e. increased EAT downtime, impacts fatigue performance and remaining service life under different fallback conditions.

5.3.3.1. NR baseline, Figure 17a. When evaluating whether to implement an EAT or EPT system on a bridge currently lacking both, a comparative analysis of Remaining Useful Life (RUL) extension and associated costs offers a rational decision-making framework. The baseline fatigue life improvement achievable through passive pre-tensioning can be inferred from the 0% ASU condition in the EAT-NO1 curve of Figure 17a, which effectively reflects the performance of an EPT system alone. To assess the added value of the EAT system, its incremental contribution to RUL is evaluated relative to this EPT baseline, with consideration of its behaviour during periods of downtime:

- EAT-NO1: If the EAT system defaults to EPT functionality during downtime, the RUL values are taken from the EAT-NO1 scenario.
- EAT-NO2: If no fallback mechanism is available and the EAT system is non-functional during downtime, the relevant RUL values correspond to the EAT-NO2 scenario.

Relative to the NR baseline, EAT with EPT fallback (EAT-NO1) offers orders-of-magnitude improvements in RUL, particularly at high ASU values. In contrast, the performance of EAT without fallback (EAT-NO2) is markedly

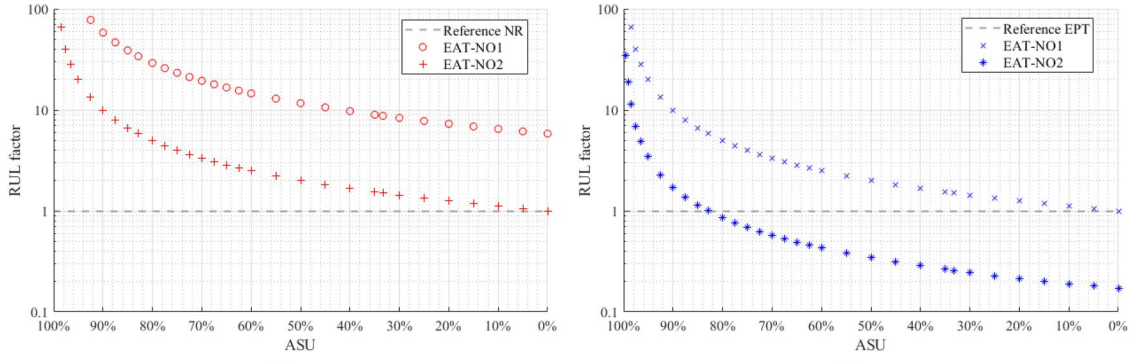

Figure 17. RUL based on Active System Utilisation: (a) NR baseline, (b) EPT baseline; 100% ASU → always functional, 0% ASU → always down.

lower, with the RUL benefit diminishing rapidly as ASU decreases.

5.3.3.2. EPT baseline, Figure 17b. Compared to the EPT system baseline shown in Figure 17b, the relative advantages of the EAT system diminish as ASU decreases. At low ASU levels, the RUL ratio approaches that of the EPT baseline, indicating minimal additional benefit. While an EPT fallback configuration (EAT-NO1) offers partial mitigation of downtime effects, the full performance gains of the EAT system are only realised when ASU exceeds approximately 82.5%. Below this threshold, system reliability becomes a limiting factor, particularly in the absence of fallback mechanisms, as in the EAT-NO2 scenario. These findings remain consistent across ± 1 category variation in FAT-class assumptions, confirming the robustness of the assessment. Furthermore, system effectiveness varies with FAT class: lower classifications diminish EPT (EAT-NO1) benefits while amplifying EAT performance gains, demonstrating EAT's superior resilience under more demanding conditions.

6. Discussion

6.1. Practical implementation and operational robustness

Translating EAT from simulation to field deployment entails addressing practical aspects related to sensing, control robustness, and hardware reliability. Real-time control depends on accurate state information, which in practice can be achieved using a combination of displacement or strain sensors and disturbance estimators as demonstrated by Zeller et al. (2023). Since sensor and actuator faults may occur, robust and fault-tolerant control algorithms, such as model-predictive or gain-scheduled LQR controllers with redundancy in the measurement and actuation networks, are essential to maintain stability under partial system degradation.

In the present context, redundancy can be implemented both physically and algorithmically. Physically, redundant actuators or load-sharing mechanisms among struts can prevent local overstressing in case of a single actuator failure. Algorithmically, fallback modes corresponding to reduced control authority (as modelled through the EAT-NO1 and EAT-NO2 cases) ensure that the bridge remains safe and serviceable even when the adaptive system is temporarily inactive. Control robustness is further supported by systematic calibration of the control gains against modelling uncertainties and environmental variability, following the adaptive control and MPC approaches tested by Dakova et al. (2023). Integration with existing monitoring systems also enables periodic health checks of the electromechanical components, limiting unplanned downtime. In addition, the hierarchical two-step framework used in this study, where control forces are derived from a reduced 2D model and applied to the high-fidelity 3D representation, provides a computationally practical basis for implementation in digital-twin environments, facilitating continuous model updating and predictive maintenance planning.

6.2. Reliability perspective and system availability

This study's fatigue assessment assumes theoretically infinite life when stress amplitudes remain below the fatigue strength threshold, yet experimental evidence suggests damage can still accumulate under such conditions (Bathias, 1999). The Eurocode 3 (CEN, 2005b) framework adopted here does not account for mean stress effects or distinguish between tensile and compressive ranges, unlike the FKM guideline which incorporates mean stress through approaches such as Haigh diagrams (Rennert, 2020). While the nominal stress method aligns with Eurocode provisions, it may under- or overestimate damage depending on detail geometry (Haibach, 2006). More advanced notch stress or fracture mechanics approaches could provide enhanced local accuracy but require extensive weld modelling, finer meshes, and significantly higher computational costs. Nevertheless, the uncertainty introduced by the nominal stress approach is comparatively small relative to that arising from traffic loading variability, simplified boundary conditions, and material property scatter.

This study examines the interaction between adaptive control interventions and fatigue damage, explicitly incorporating EAT system downtimes through the Active System Utilisation (ASU) metric. ASU is applied as a concise, standardised measure of system availability rather than a full probabilistic reliability model. Although broader lifecycle interactions, such as material degradation, traffic variability, or seismic events, were not addressed, they underline the potential for extending this framework towards probabilistic reliability and resilience analyses in future work, thereby enhancing predictive robustness and supporting more informed design and maintenance strategies for adaptive retrofitted bridge systems.

7. Conclusions

This study demonstrates that External Adaptive Tensioning (EAT) systems significantly reduce the stress response, by approximately 66% relative to the unretrofitted case, and nearly eliminate fatigue damage across all critical locations under typical operational scenarios. By introducing the concept of Active System Utilisation (ASU), the analysis quantifies how system reliability and fallback configurations affect long-term performance, underscoring the need for robust maintenance strategies and fail-safe mechanisms to maximise operational benefits. Compared to the localised and often uneven improvements offered by passive retrofit systems, EAT provides consistently superior fatigue mitigation, significantly extending the remaining service life of ageing steel bridges.

Beyond direct fatigue benefits, the results highlight the structural value of adaptivity in retrofit strategies. By dynamically redistributing internal forces, EAT systems more effectively address both global and local stress

concentrations than passive post-tensioning, helping to avoid detrimental effects such as stress reversal or unintended amplification, phenomena sometimes observed in conventional approaches. These findings support the role of adaptivity as a key enabler of improved safety, durability, and serviceability in bridge retrofitting.

Future work should incorporate probabilistic models to capture uncertainties in loading, material degradation, and system reliability. Experimental validation of numerical predictions will also be essential to demonstrate feasibility under real-world conditions. Additionally, optimisation of actuator placement and control logic could further improve performance while minimising operational demands. Together, these avenues offer a strong foundation for advancing adaptive retrofitting as a reliable and effective solution for extending the service life of bridge infrastructure.

Acknowledgements

The authors gratefully acknowledge the German Research Foundation (DFG) for its core support through the Collaborative Research Center CRC 1244, *Adaptive Skins and Structures for the Built Environment of Tomorrow* (Grant No. 279064222). They also thank Dr. Arka P. Reksowardojo and Mr. Keiya Nakazato of ILEK, University of Stuttgart, for their assistance in developing the structural analysis models employed in this study.

Author contributions

CRediT: **Dshamil Efinger**: Data curation, Formal analysis, Investigation, Methodology, Software, Validation, Visualization, Writing – original draft; **Khairina A. Canny**: Data curation, Formal analysis, Investigation, Methodology, Validation, Visualization, Writing – original draft; **Martin Dazer**: Funding acquisition, Supervision; **Lucio Blandini**: Funding acquisition, Project administration, Resources; **Gennaro Senatore**: Conceptualization, Formal analysis, Investigation, Methodology, Project administration, Resources, Software, Supervision, Validation, Visualization, Writing – original draft, Writing – review & editing.

Disclosure statement

No potential conflict of interest was reported by the author(s).

Funding

This work was supported by the Collaborative Research Center CRC 1244 "Adaptive Skins and Structures for the Built Environment of Tomorrow" (Deutsche Forschungsgemeinschaft, Grant No. 279064222).

References

Alsharari, F., El-Zohairy, A., Salim, H., & El-Din El-Sisi, A. (2021). Pre-damage effect on the residual behavior of externally post-tensioned fatigued steel-concrete composite beams. *Structures*, *32*, 578–587. https://doi.org/10.1016/j.istruc.2021.02.064

Avci, O., Abdeljaber, O., Kiranyaz, S., Hussein, M., Gabbouj, M., & Inman, D. J. (2021). A review of vibration-based damage detection in civil structures: From traditional methods to machine learning and deep learning applications. *Mechanical Systems and Signal Processing*, *147*, 107077. https://doi.org/10.1016/j.ymssp.2020.107077

Banerjee, T., Ghosh, D., & Das, D. (2025). A state-of-the-art review and future challenges on application of devices for vibration control of bridges. *Mechanics of Advanced Materials and Structures*, 1–27. https://doi.org/10.1080/15376494.2025.2462713

Bathias. (1999). There is no infinite fatigue life in metallic materials. *Fatigue & Fracture of Engineering Materials & Structures*, *22*(7), 559–565. https://doi.org/10.1046/j.1460-2695.1999.00183.x

Bažant, Z. P., Yu, Q., & Li, G.-H. (2012). Excessive Long-Time Deflections of Prestressed Box Girders. I: Record-Span Bridge in Palau and Other Paradigms. *Journal of Structural Engineering*, *138*(6), 676–686. https://doi.org/10.1061/(ASCE)ST.1943-541X.0000487

Bertolesi, E., Buitrago, M., Adam, J. M., & Calderón, P. A. (2021). Fatigue assessment of steel riveted railway bridges: Full-scale tests and analytical approach. *Journal of Constructional Steel Research*, *182*, 106664. https://doi.org/10.1016/j.jcsr.2021.106664

Burgoyne, C., & Scantlebury, R. (1996). Why did Palau Bridge collapse? *The Structural Engineer*, *74*(11), 177–186.

Canny, K. A., Senatore, G., & Blandini, L. (2025). Investigation of retrofit strategies to extend the service life of bridge structures through active control. *Journal of Bridge Engineering*, *30*(2), 04024109. https://doi.org/10.1061/JBENF2.BEENG-6925

Cao, S., Ozbulut, O. E., Shi, F., & Deng, J. (2022). Experimental and numerical investigations on hysteretic response of a multi-level SMA/lead rubber bearing seismic isolation system. *Smart Materials and Structures*, *31*(3), 035024. https://doi.org/10.1088/1361-665X/ac4f20

CEN. (2003). *Eurocode 1 (EN 1991-2): Actions on structures – Part 2: Traffic loads on bridges*.

CEN. (2005a). *Eurocode 3 (EN 1993-1-2): Design of steel structures – General rules – Structural fire design*.

CEN. (2005b). *Eurocode 3 (EN 1993-1-9): Design of steel structures – Part 1-9. Fatigue*.

Chen, B., Zhang, Z., & Hua, X. (2022). Equal modal damping-based optimal design of a grounded tuned mass-damper-inerter for flexible structures. *Structural Control and Health Monitoring*, *29*(12), e3106. https://doi.org/10.1002/stc.3106

Chen, Z. Q., Wang, X. Y., Ko, J. M., Ni, Y. Q., Jr, Spencer, B. F., & Yang, G. (2003). MR damping system on Dongting Lake cable-stayed bridge. *Smart Structures and Materials 2003: Smart Systems and Nondestructive Evaluation for Civil Infrastructures*, *5057*, 229–235. https://doi.org/10.1117/12.498072

Dai, J., Xu, Z.-D., & Dyke, S. J. (2022). Robust control of vortex-induced vibration in flexible bridges using an active tuned mass damper. *Structural Control and Health Monitoring*, *29*(8), e2980. https://doi.org/10.1002/stc.2980

Dakova, S., Zeller, A., Reksowardojo, A. P., Senatore, G., Böhm, M., Blandini, L., & Sawodny, O. (2023). A model predictive control strategy for adaptive railway bridges. *IFAC-PapersOnLine*, *56*(2), 7686–7691. https://doi.org/10.1016/j.ifacol.2023.10.1170

Delzendeh Moghadam, M., Fathi, A., & Chaallal, O. (2024). Retrofitting of steel structures with CFRP: Literature review and research needs. *Applied Sciences*, *14*(13), 5958. https://doi.org/10.3390/app14135958

Du, G., Brincker, R., Amador, S., & Alibrandi, U. (2024). OMA-driven structural assessment to prevent fatigue-induced failure in steel bridges. In *Bridge maintenance, safety, management, digitalization and sustainability*. CRC Press.

Ebeling, C. (2019). *An introduction to reliability and maintainability engineering* (3rd ed.). Waveland Press, Inc.

Eberle, R., & Oberguggenberger, M. (2023). Vibrations of a bridge with random structural irregularities under random traffic load and a probabilistic structural degradation assessment approach. *Journal of Vibration Engineering & Technologies*, *11*(4), 1851–1865. https://doi.org/10.1007/s42417-022-00675-w

Efinger, D., Ostertag, A., Dazer, M., Borschewski, D., Albrecht, S., & Bertsche, B. (2022). Reliability as a key driver for a sustainable design of adaptive load-bearing structures. *Sustainability*, *14*(2), 895. https://doi.org/10.3390/su14020895

Fatemi, A. A., Tabrizian, Z., Amiri, G. G., & Beigi, M. H. A. (2011). Steel bridges retrofitting techniques. *International Journal of Earth Sciences and Engineering*, *04*(06), 695–698.

Frangopol, D. M., & Kim, S. (2022). *Bridge safety, maintenance and management in a life-cycle context*. CRC Press. https://doi.org/10.1201/9781003196877

Gkatzogias, K. I., & Kappos, A. J. (2016). Semi-active control systems in bridge engineering: A review of the current state of practice. *Structural Engineering International*, *26*(4), 290–300. https://doi.org/10.2749/101686616X14555429844040

Haibach, E. (2006). *Betriebsfestigkeit: Verfahren und Daten zur Bauteilberechnung* (3. Auflage). Springer. http://site.ebrary.com/lib/hsalbsig/docDetail.action?docID=10183104

Horgan, R. (2021). Is seismic retrofit to blame for 'unusual' failure in Mississippi River bridge. *New Civil Engineer*. https://www.newcivilengineer.com/latest/is-seismic-retrofit-to-blame-for-unusual-failure-in-mississippi-river-bridge-14-05-2021/

Kalkowsky, F., Schröder, M., Blunk, C., Glienke, R., Alex, J., & Flügge, W. (2024). Remaining fatigue strength of an orthotropic steel deck with respect to a repair method by cold joining techniques. *ce/papers*, *7*(3-4), 143–152. https://doi.org/10.1002/cepa.3079

Li, Y., Hu, D., Xu, Y., Wang, B., Zhou, Y., & Dong, Z. (2025). Study on the mechanical behavior of corroded bridge steel based on the entire process of tensile failure. *Materials Research Express*, *12*(1), 016514. https://doi.org/10.1088/2053-1591/adaac2

Møller, R. N., Krenk, S., & Svendsen, M. N. (2019). Damping system for long-span suspension bridges. *Structural Control and Health Monitoring*, *26*(12), e2448. https://doi.org/10.1002/stc.2448

Reksowardojo, A. P., & Senatore, G. (2023). Design of ultra-lightweight and energy-efficient civil structures through shape morphing. *Computers & Structures*, *289*, 107149. https://doi.org/10.1016/j.compstruc.2023.107149

Reksowardojo, A. P., Senatore, G., Bischoff, M., & Blandini, L. (2024a). Design and control benchmark of rib-stiffened concrete slabs equipped with an adaptive tensioning system. *Journal of Structural Engineering*, *150*(1), 04023200. https://doi.org/10.1061/JSENDH.STENG-12320

Reksowardojo, A. P., Senatore, G., Bischoff, M., & Blandini, L. (2024b). Design and control of high-speed railway bridges equipped with an under-deck adaptive tensioning system. *Journal of Sound and Vibration*, *579*, 118362. https://doi.org/10.1016/j.jsv.2024.118362

Rennert, R. (Ed.). (2020). *Rechnerischer Festigkeitsnachweis für Maschinenbauteile aus Stahl, Eisenguss- und Aluminiumwerkstoffen* (7., überarbeitete Auflage). VDMA Verlag.

Saeed, A. S., Abdul Nasar, R., & Al-Shudeifat, M. A. (2023). A review on nonlinear energy sinks: Designs, analysis and applications of impact and rotary types. *Nonlinear Dynamics*, *111*(1), 1–37. https://doi.org/10.1007/s11071-022-08094-y

Senatore, G., & Wang, Y. (2024). Topology optimization of adaptive structures: New limits of material economy. *Computer Methods in Applied Mechanics and Engineering*, *422*, 116710. https://doi.org/10.1016/j.cma.2023.116710

Senatore, G., Virgili, F., & Blandini, L. (2025). Global optimal actuator placement for adaptive structures: New formulation and benchmarking. *Journal of Intelligent Material Systems and Structures*, *36*(3), 151–173. https://doi.org/10.1177/1045389x241293861

Soliman, M., & Frangopol, D. M. (2015). Life-cycle cost evaluation of conventional and corrosion-resistant steel for bridges. *Journal of Bridge Engineering*, *20*(1), 06014005. https://doi.org/10.1061/(ASCE)BE.1943-5592.0000647

Tell, S., Leander, J., Andersson, A., & Ülker-Kaustell, M. (2021). Probability-based evaluation of the effect of fluid viscous dampers on a high-speed railway bridge. *Structure and Infrastructure Engineering*, *17*(12), 1730–1742. https://doi.org/10.1080/15732479.2020.1832537

van Dinter, R., Tekinerdogan, B., & Catal, C. (2022). Predictive maintenance using digital twins: A systematic literature review. *Information and Software Technology*, *151*, 107008. https://doi.org/10.1016/j.infsof.2022.107008

Wang, Q., Senatore, G., Jansen, K., Habraken, A., & Teuffel, P. (2021). Seismic control performance of a three-story frame prototype equipped with semi-active variable stiffness and damping structural joints. *Earthquake Engineering & Structural Dynamics*, *50*(13), 3379–3402. https://doi.org/10.1002/eqe.3514

Wang, R., Leander, J., & Karoumi, R. (2023). Fatigue reliability assessment of steel bridges considering spatial correlation in system evaluation. *Structure and Infrastructure Engineering*, *19*(2), 254–268. https://doi.org/10.1080/15732479.2021.1938614

Wang, Z., Zhao, L., Chen, H., Fang, G., Li, K., & Ge, Y. (2023). Flutter control of active aerodynamic flaps mounted on streamlined bridge deck fairing edges: An experimental study. *Structural Control and Health Monitoring*, *2023*(1), 1–16. https://doi.org/10.1155/2023/9970603

Wei, X., Ngeljaratan, L., & Bruneau, M. (2019). Low-cycle fatigue of buckling restrained braces in bidirectional ductile end diaphragms due to temperature-change effect on bridge superstructure. *Journal of Bridge Engineering*, *24*(4), 04019014. https://doi.org/10.1061/(ASCE)BE.1943-5592.0001365

Wu, C., Zhang, Z., & Chen, Z. (2018). Stiffness degradation of suspension bridges and refined analysis of aerodynamic torsional divergence. *Advances in Structural Engineering*, *21*(6), 877–890. https://doi.org/10.1177/1369433217734018

Yang, C., Wang, H., Xie, L., Li, A., & Wang, X. (2024). Experimental and theoretical investigations on an asynchronized parallel double-stage viscous fluid damper. *Structural Control and Health Monitoring*, *2024*(1), 6921518. https://doi.org/10.1155/2024/6921518

Yang, Y.-B., Yau, J.-D., & Hsu, L.-C. (1997). Vibration of simple beams due to trains moving at high speeds. *Engineering Structures*, *19*(11), 936–944. https://doi.org/10.1016/S0141-0296(97)00001-1

Yoon, S., Spencer, B. F., Jr., Lee, S., Jung, H.-J., & Kim, I.-H. (2022). A novel approach to assess the seismic performance of deteriorated bridge structures by employing UAV-based damage detection. *Structural Control and Health Monitoring*, *29*(7), e2964. https://doi.org/10.1002/stc.2964

Zeller, A., Dakova, S., Stein, C., Böhm, M., Senatore, G., Reksowardojo, A. P., Blandini, L., Sawodny, O., & Tarín, C. (2023). Bridge state and average train axle mass estimation for adaptive railway bridges. *IEEE/ASME Transactions on Mechatronics*, *28*(4), 1880–1889. https://doi.org/10.1109/TMECH.2023.3277317

Zhang, K., Qi, T., Li, D., Xue, X., & Zhu, Z. (2021). Load testing and health monitoring of monolithic bridges with innovative reinforcement. *International Journal of Structural Integrity*, *12*(6), 904–921. https://doi.org/10.1108/IJSI-11-2020-0103